

THESIS
1
2001



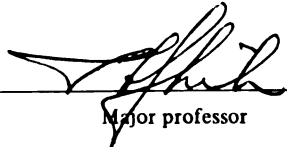
This is to certify that the
thesis entitled
**BLEED BOUNDARY CONDITIONS FOR CFD SIMULATIONS OF
SUPERSONIC FLOWS WITH BOUNDARY-LAYER BLEED**

presented by

David Benjamin Benson

has been accepted towards fulfillment
of the requirements for

M.S. degree in Mechanical Engineering



Major professor

Date Aug. 21, 2001

PLACE IN RETURN BOX to remove this checkout from your record.
TO AVOID FINES return on or before date due.
MAY BE RECALLED with earlier due date if requested.

DATE DUE	DATE DUE	DATE DUE

**BLEED BOUNDARY CONDITIONS FOR CFD SIMULATIONS OF SUPERSONIC
FLOWS WITH BOUNDARY-LAYER BLEED**

By

David Benjamin Benson

A THESIS

**Submitted to
Michigan State University
in partial fulfillment of the requirements
for the degree of**

MASTER OF SCIENCE

Department of Mechanical Engineering

2001

ABSTRACT

**BLEED BOUNDARY CONDITIONS FOR CFD SIMULATIONS OF SUPERSONIC
FLOWS WITH BOUNDARY-LAYER BLEED**

By
David Benjamin Benson

In CFD simulations of supersonic flows, where bleed through discrete holes is used to control boundary-layer profiles, resolving the flow through each bleed hole and the bleed plenum can require a prohibitively large number of grid points. In this study, four outflow boundary conditions (BCs) for bleed holes, referred to as bleed BCs, were developed so that bleed holes and plenums need not be simulated. The usefulness of the bleed BCs developed was evaluated by comparing with simulations that resolved the flow in each hole and plenum (referred to as “DNS results”). The four bleed BCs developed are: DNS-BC (specify normal velocity, W , at bleed-hole locations based on DNS results and extrapolate all other dependent variables), Cd-BC (same as DNS-BC except W is calculated by using a discharge coefficient), W-Avg (same as DNS-BC except specify a constant W), and W-Profile (same as W-Avg except that W is allowed two values). Results obtained show that all bleed BCs developed can predict accurately the pressure and Mach number profiles downstream of the bleed region. For Cd-BC, it was shown that the number of grid points needed to resolve a bleed hole can be as few as one for normal holes and two for inclined holes, and still get accurate results and capture the qualitative features of the bleed process.

“Laughter is wine for the soul - laughter soft, or loud and deep, tinged through with seriousness.... the hilarious declaration made by man that life is worth living.”
- Sean O’Casey

ACKNOWLEDGEMENTS

This work was supported by NASA grant NAG 3-2234 from NASA - Glenn Research Center and the CRAY computer time was provided by the NASA's NAS Facility. The author is especially grateful for their support.

I would also like to thank my advisor, Dr. Tom I.P. Shih for providing the opportunity to work in the area of inlets and boundary-layer control/modeling, Dr. Yu-liang Lin for his patience and assistance in helping me with many aspects of programming and Dr. Robert Stein for the UNIX indoctrination.

TABLE OF CONTENTS

LIST OF TABLES	vi
LIST OF FIGURES	vii
NOMENCLATURE	ix
CHAPTER 1 BACKGROUND.....	1
CHAPTER 2 PROBLEM DESCRIPTION	5
CHAPTER 3 GOVERNING EQUATIONS	11
CHAPTER 4 BOUNDARY CONDITION FORMULATION	15
CHAPTER 5 NUMERICAL METHOD OF SOLUTION	19
CHAPTER 6 RESULTS	24
CHAPTER 7 CONCLUSION	51
REFERENCES	53

LIST OF TABLES

Table 1: Summary of bleed-hole geometry and arrangement	10
Table 2: Grid dimensions and total number of grid points for the cases studied	21
Table 3: Bleed-boundary conditions applied and mesh refinement	38
Table 4: Summary of bleed rates and discharge coefficients for each bleed-hole	39

LIST OF FIGURES

Figure 1: A schematic diagram of the bleed process	3
Figure 2: Schematic diagram of bleed holes and plenum	5
Figure 3: Schematic diagram of the arrangement of bleed holes on the surface for $M=2.46$ case (normal holes)	7
Figure 4: Schematic diagram of the arrangement of bleed holes on the surface for $M=1.6$ (case #3 and case #4, Table 1)	8
Figure 5: Schematic diagram of the arrangement of bleed holes on the surface for $M=1.6$ (case #5, Table 1)	8
Figure 6: Schematic diagram of the arrangement of bleed holes on the surface for $M=1.6$ (case #6, Table 1)	9
Figure 7: Fine H-H grid above plate, plate surface (top) and side view. In the top view, the lighter shade of grey regions represent hole locations	22
Figure 8: Coarse H-H grid above plate, plate surface (top) and side view. In the top view, the lighter shade of grey regions represent hole locations	23
Figure 9: DNS results for pressure contours in left symmetry plane and on plate surface with velocity vectors at $z = 10^{-5}$ m above the plate	25
Figure 10: Pressure contours in left symmetry plane and on plate surface for different bleed BCs	27
Figure 11: Separation downstream – W_{Avg} and Cd_{BC} boundary conditions	28
Figure 12: Mach number profile across third row of normal holes	29
Figure 13: Normalized pressure profile across third row of normal holes	30
Figure 14: Normal velocity (W) profile across third row of normal holes	31
Figure 15: Mach number profile 1D downstream of last row of holes	33
Figure 16: Normalized pressure profile 1D downstream of last row of holes	34

Figure 17: Contour plots of pressure for the DNS results (upper) and coarse grid case (lower)	35
Figure 18: Pressure and Mach number profiles 1D downstream of last row of holes – coarse case	36
Figure 19: Mach contours in left symmetry plane and on plate surface of the DNS results for all of the cases	41
Figure 20: Mach number contours in left symmetry plane ($y = L_y$) and on plate surface ($z = 0$) for Case 5 and DNS, DNS_BC, and Cd_BC. Contour level same as B in Fig. 19	42
Figure 21: Normalized pressure along middle of 3 rd row hole at $z = 0$ (plate surface) for DNS, DNS_BC, and Cd_BC	43
Figure 22: Mach number along middle of 3 rd row hole at $z = 0$ (plate surface) for DNS, DNS_BC, and Cd_BC	44
Figure 23: Mach number at 1D downstream of last-row holes for DNS, DNS_BC, and Cd_BC	45
Figure 24: Normalized pressure at 1D downstream of last-row holes for DNS, DNS_BC, and Cd_BC	46
Figure 25: Pressure contours in left symmetry plane ($y = L_y$) and on plate surface ($z = 0$) for Cases 3 and 4 with Cd_BC on fine and coarse meshes and Cd_BC-slot on coarse mesh	49
Figure 26: Mach number and pressure profile normal to wall at $y = 0$ and 1D downstream of last row holes for Cases 3 and 4 with Cd_BC on fine and coarse meshes and Cd_BC-slot on coarse mesh. Reference refer to DNS results	50

NOMENCLATURE

C_D	discharge coefficient
D	bleed-hole diameter
\hat{e}	mechanical plus thermal energy per unit volume
k	turbulent kinetic energy
L_x	streamwise bleed-hole spacing
L_y	spanwise bleed-hole spacing
m_b	mass-flow rate through bleed-hole
M_∞	freestream Mach number
P	static pressure
P_b	plenum exit static pressure
P_∞	freestream static pressure
q_i	Fourier conduction in the i -th direction
T_∞	freestream static temperature
W	velocity normal to the plate

Greek

α	angle of the bleed-holes with respect to the plate
β	plenum angle
Δy	normal distance of first grid point from the wall
γ	ratio of specific heats
μ	viscosity
Θ	angle between centers of bleed holes
ρ	density
τ_{ij}	combined laminar and turbulent shear stress
ω	dissipation rate per unit of turbulent kinetic energy
Ω	vorticity
ξ	normal distance from solid wall

Chapter 1

INTRODUCTION

For many aerodynamic devices that operate in the supersonic regime, boundary-layer distortion due to surface curvature and incident shock waves is controlled by bleeding away the low-momentum air next to the wall into a plenum through discrete holes. Since bleed removes air that can produce useful work and the bleeding process requires work input, a major goal is to design bleed systems that can provide effective control with minimum bleed.

Computational fluid dynamics (CFD) is a promising design and analysis tool for bleed systems. With computational fluid dynamics, two approaches are possible for analyzing bleed systems. The first approach is to simulate the flow in the entire bleed system, including the flow through each bleed hole and the plenum.¹⁻¹⁰ The advantage of this approach is that the physics of the bleed process is simulated by using first principles. The disadvantage, however, is that a very large number of grid points or cells are needed to resolve the flow in the holes and the plenum. The second approach is to model, instead of simulate, the flow through the bleed holes and the plenum. This is accomplished by using what are referred to as bleed boundary conditions, which are applied to surfaces only where bleed is desired.¹¹⁻¹⁶ This approach requires substantially fewer grid points since the bleed holes and plenum are not resolved. With fewer grid points, the researcher benefits from greatly reduced memory and CPU-time requirements. An additional benefit of this method is the ability to easily change the bleed hole configuration without having to make extensive modifications to the grid structure for the

problem. The approach based on bleed boundary conditions is, therefore, preferred from both a computational efficiency and an ease of design point of view. Its usefulness, however, hinges on the accuracy of the bleed boundary conditions used in modeling the relevant physics.

To date, all bleed boundary conditions have treated each bleed patch (i.e. a region with bleed holes) as a porous surface.¹¹⁻¹⁶ With such a model, information on hole geometry and arrangement are not represented. The focus of these bleed boundary conditions has been on predicting the correct bleed rate. While the bleed rate may be the most important part of the bleed process, by disregarding the bleed-hole geometry and arrangement, some aspects of bleeding a supersonic boundary layer are lost in the analysis. In particular, the “barrier” shocks inside the bleed holes and their influences on boundary-layer control are not accounted for in these models.¹⁷ Paynter, et al.¹⁴ and Lee, et al.¹⁵ improved upon the porous-wall type bleed boundary condition by adding a partial differential equation that resembles a one-equation turbulence model to include the roughness effects induced by the bleed process.

Some of the key flow features observed in shock-wave/boundary-layer interactions with bleed through circular holes were identified in a paper by Shih, et al.¹⁷. One of the key features identified by Shih, et al. is that a “barrier” shock is formed in and around each bleed-hole because of the bleed process (Figure 1). The nature of the “barrier” shock in each hole was observed to depend on the pressure-ratio across the hole, the bleed-hole angle, its distance from neighboring holes and its position relative to any incident shocks. Shih, et al.¹⁷ also observed that the bleed-holes exert a spanwise influence on the flow when rows of holes are arranged in a staggered fashion.

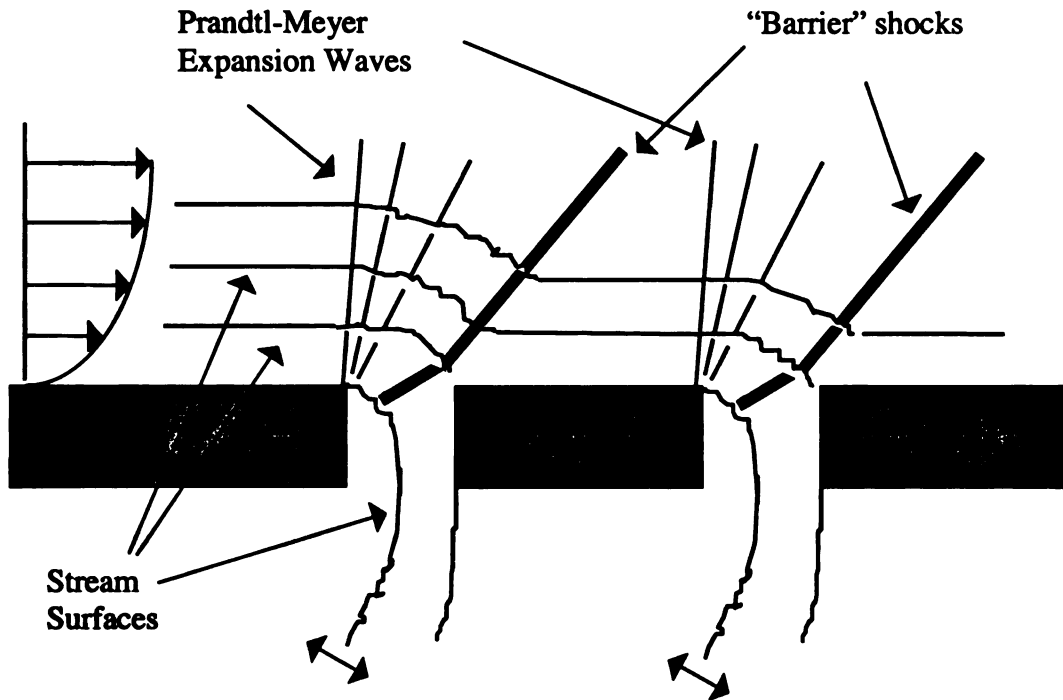


Figure 1: A schematic diagram of the bleed process

The design of a bleed system for controlling a supersonic boundary layer flow can be a difficult endeavor because of the numerous interactions that can occur between the boundary layer and the bleed process. In addition to the complex flow structures that are observed, numerous design configurations are also possible. Flow through the holes can be choked or not depending on the back pressure at the plenum exit. The holes can be oriented normal to the bleed surface or inclined at some angle. The streamwise and spanwise spacing as well as the pattern of the holes in the bleed region can be varied. Another complication that exists is that there are numerous classes of flows where accurate bleed is critical for stability. For example, in situations where there is an incident shock wave impinging on the boundary layer, the adverse pressure gradient induced by the shock can cause flow separation. Boundary-layer bleed can be utilized as

a way of controlling the undesirable effects of shock-wave/boundary-layer in regions where shock waves impinge on the boundary layer.

The objective of this study is twofold. The first is to develop and evaluate bleed boundary conditions for CFD analysis of bleed systems that are able to account for bleed-hole geometry and arrangement. The second is to perform a sensitivity study on how coarse the grid can be and still enable bleed boundary conditions to predict the correct boundary-layer profile downstream of the bleed region.

The focus of this study is on choked bleed of a supersonic boundary layer on a flat plate with and without an incident shock wave through rows of normal and inclined holes that are arranged in a staggered fashion. The bleed boundary conditions developed will be evaluated by comparing predictions with simulations that resolved the flow through the bleed holes and the plenum. In this study, simulations that resolve the flow through the bleed holes and the plenum are referred to as “DNS results” because the geometry is resolved instead of modeled though turbulence is still modeled through the ensemble average approach.

Chapter 2

PROBLEM DESCRIPTION

The flows studied involve a supersonic turbulent boundary layer flow on a flat plate in which the fluid (air) next to the plate is bled in to a plenum through rows of circular holes arranged in a staggered fashion. Figure 2 shows a schematic of the problem.

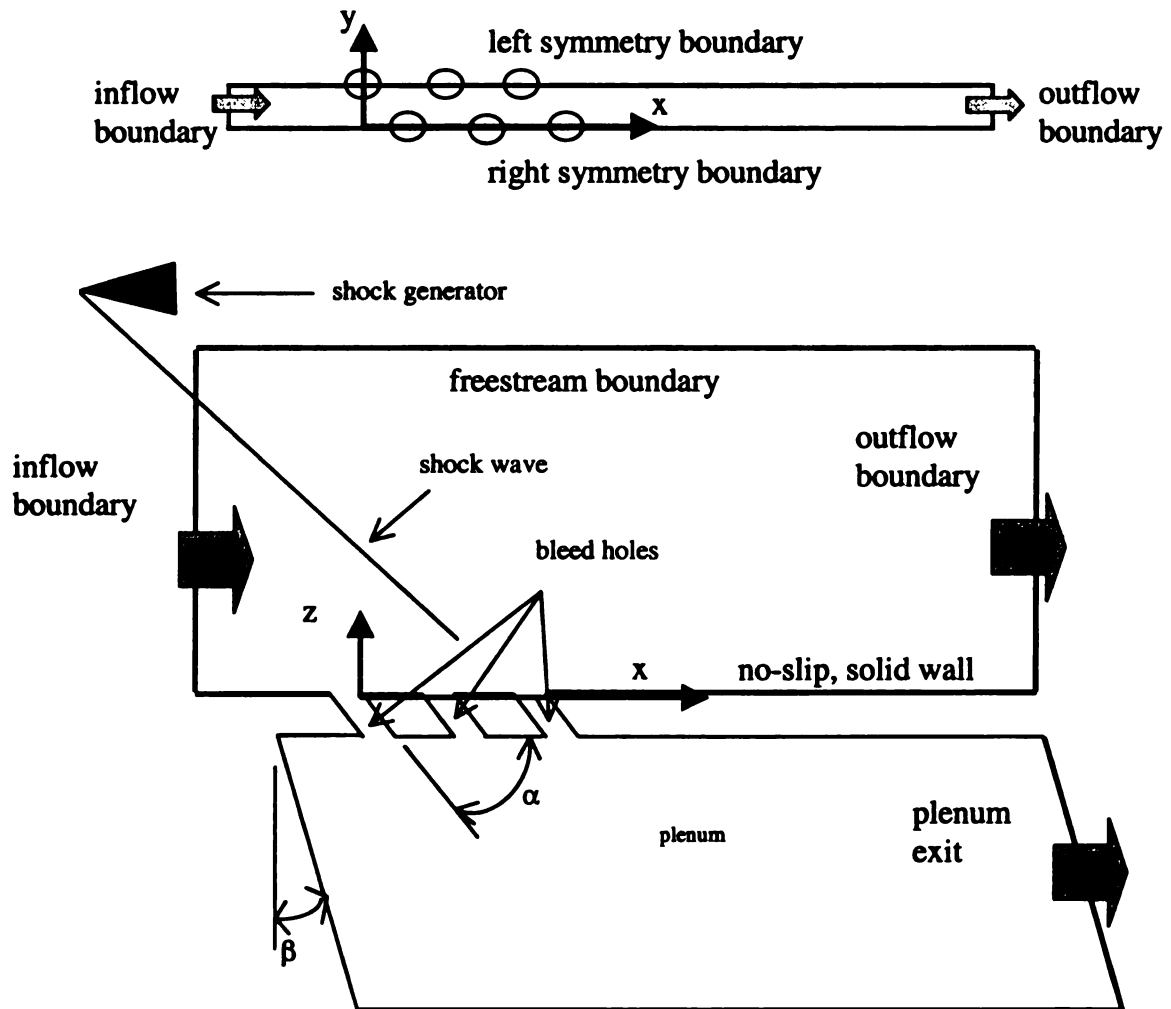


Figure 2: Schematic diagram of bleed holes and plenum.

For the boundary layer flow above the plate, two free stream Mach numbers, M_∞ , were simulated: $M_\infty = 2.46$ and $M_\infty = 1.6$. When $M_\infty = 2.46$, there were no incident shock waves. The corresponding freestream static temperature, T_∞ , and pressure, P_∞ , were 132.56 K and 10.7 kPa respectively and the momentum boundary-layer thickness just upstream of the bleed region was 0.198. When $M_\infty = 1.6$, simulations were conducted for flow over a flat plate with and without an incident shock wave. For this freestream Mach number, the corresponding freestream static temperature, T_∞ , and pressure, P_∞ , were 300 K and 61.32 kPa respectively. For the simulations where there is an incident shock, the shock generator, a wedge with half angle of 7.5° , was positioned so that the incident shock always impinges along a line on the plate that passes through the middle of the third-row holes under the condition of uniform flow. However, since the flow is non-uniform because of the boundary layer, the actual incident location simulated is slightly upstream of the middle of the third-row holes.

Five different bleed-hole configurations were simulated for this research. They differ in their hole inclination (normal with $\alpha = 90^\circ$, inclined with $\alpha = 20^\circ$), the number of rows of holes present (four rows and six rows), and in the spacing between holes along both the x (streamwise) and y (spanwise) directions. For all of the simulations that resolved the flow through the holes and the plenum, the back pressure P_b at the plenum exit was maintained low enough to ensure choked flow through the bleed holes. For the $M_\infty = 2.46$ cases, $P_b / P_\infty = 0.25618$ for normal holes and 0.75888 for inclined holes. For the $M_\infty = 1.6$ cases, $P_b / P_\infty = 0.35$. When the holes are inclined with respect to the

plate ($\alpha = 20^\circ$), the plenum is tilted by an angle β , which is set equal to $\alpha/2$. For the normal holes, the plenum side walls are oriented normal to the plate surface ($\beta = 0^\circ$).

As noted, the bleed-holes studied were arranged in a staggered fashion on the plate surface. For the $M_\infty = 2.46$ simulations, two bleed-hole configurations were examined: inclined holes and normal holes. The holes had a diameter, D , of 0.625 cm. The spanwise spacing between the centers of the holes, L_y , was equal to one hole diameter and the streamwise spacing, L_x , was fixed such that $L_x = L_y * \tan \Theta$ (Figure 3). For the normal holes, $\Theta = 63.4^\circ$ ($L_x = 2D$) and for the inclined holes, $\Theta = 70.2^\circ$ ($L_x = 2.78D$).

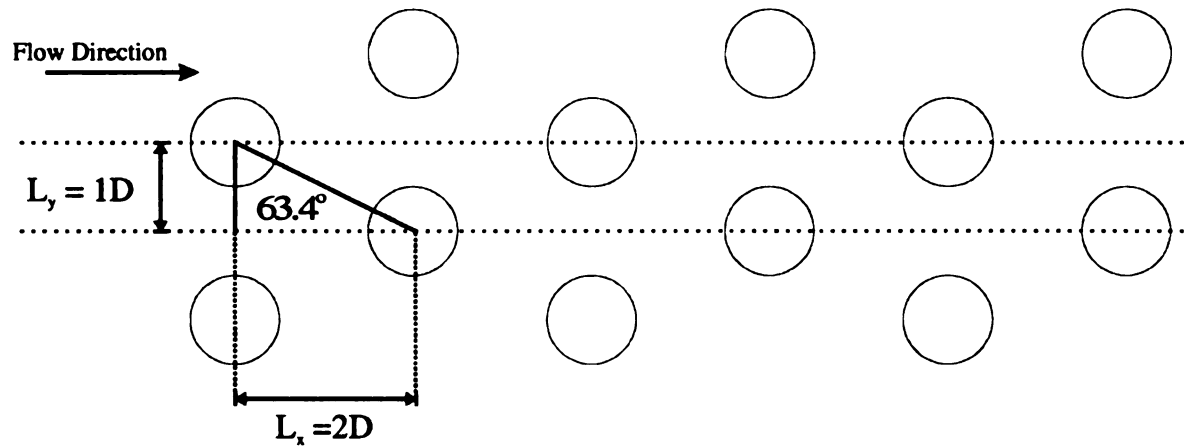


Figure 3: Schematic diagram of the arrangement of bleed holes on the surface for $M=2.46$ case (normal holes).

For the $M_\infty = 1.6$ simulations, three different bleed-hole configurations were examined, although four simulations were conducted. All of the holes considered were oriented normal to the plate surface and had a diameter of 0.508 cm. In the first configuration, the bleed holes were oriented such that the spanwise spacing was one hole

diameter ($L_y = D$) and $\Theta = 60^\circ$: this led to a streamwise spacing of $L_x = 1.73D$ (Figure 4).

Two simulations were conducted for this arrangement: one with an incident shock and the other without an incident shock (listed as case #3 and case #4 in Table 1).

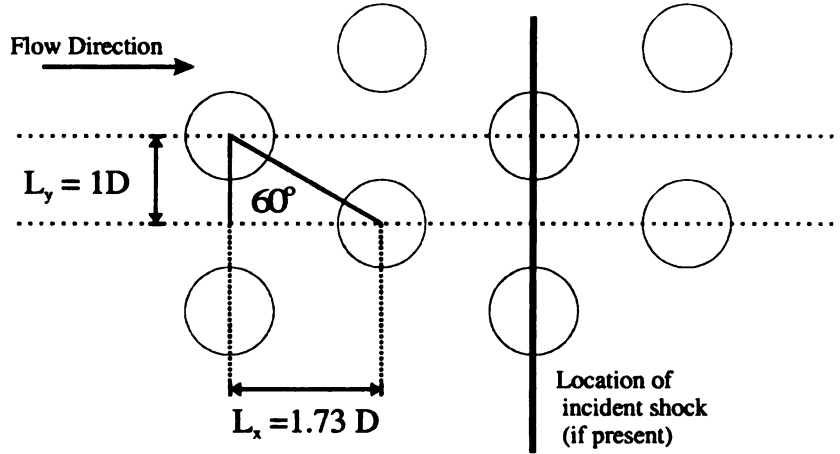


Figure 4: Schematic diagram of the arrangement of bleed holes on the surface for $M=1.6$ (case #3 and case #4, Table 1).

For the second arrangement of the bleed holes, $L_y = 1.5 D$ and $\Theta = 60^\circ$: this led to a streamwise spacing of $L_x = 2.6D$ (Figure 5). The third arrangement studied had $L_y = D$ and $\Theta = 70^\circ$: $L_x = 2.75D$ (Figure 6).

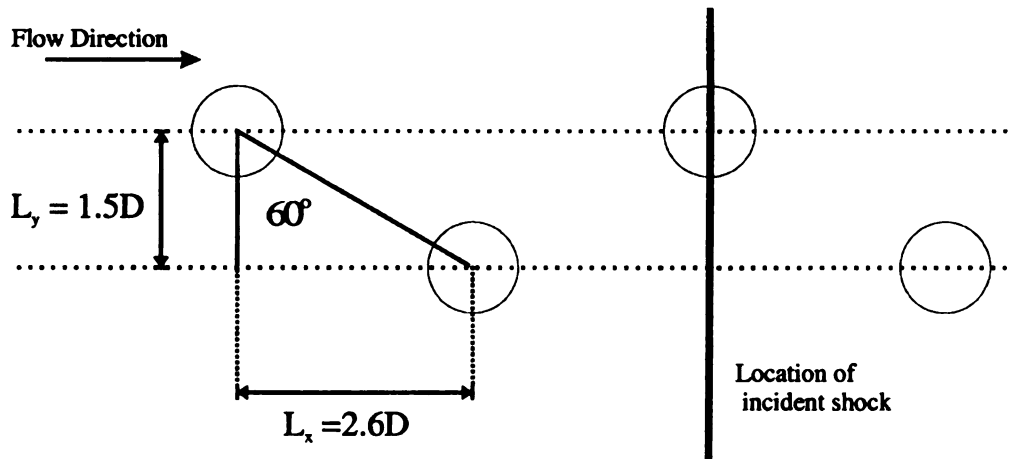


Figure 5: Schematic diagram of the arrangement of bleed holes on the surface for $M=1.6$ (case #5, Table 1).

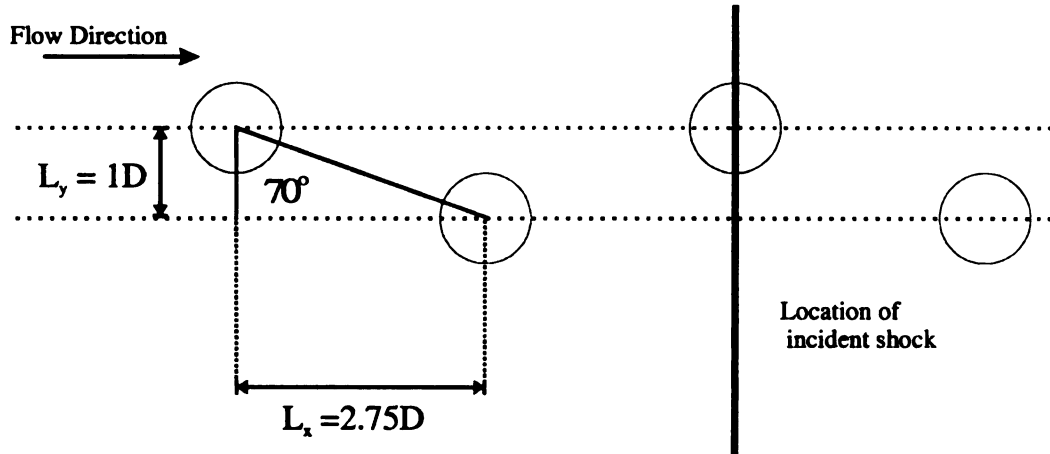


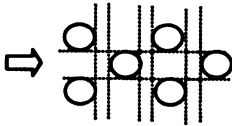
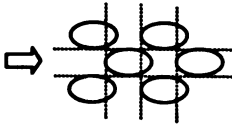
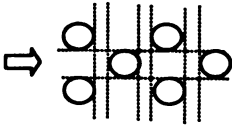
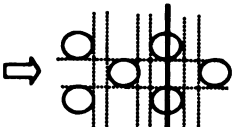
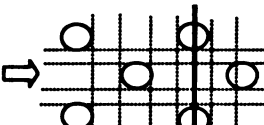
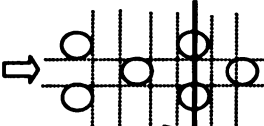
Figure 6: Schematic diagram of the arrangement of bleed holes on the surface for $M=1.6$ (case #6, Table 1).

For all of these cases, two types of simulations were performed. One type, referred to direct numerical simulation (DNS results), resolves the flow above the plate, in the holes, and in the plenum. For this type of simulation, the domain is the region bounded by the solid lines shown in the top of Figure 2. Only “half” of each bleed hole is included in the domain because of the symmetry in the spanwise direction (Figure 2). The simulations that resolved the flow through the holes and plenum were conducted by Rimlinger, et al.⁷ and Flores, et al.¹⁰

The second series of simulations conducted only resolves the flow above the flat plate and does not seek to resolve the flow in the holes and plenum. In these simulations, the flow through the holes is modeled by applying a bleed boundary condition over each bleed-hole. The bleed boundary conditions varied in the amount of information that was applied at the hole locations from the simulations that resolved the flow through the holes and plenum. Simulations were conducted on cropped versions of the grids used in the simulations that resolved the flow through the holes and plenum and on coarse grids. The

coarse grids were developed so that each hole was represented by either a single grid point/cell per hole ($\alpha = 90^\circ$) or two grid points/cells per hole ($\alpha = 20^\circ$). Table 1 is a summary of the bleed-hole geometry and arrangement information for all of the cases studied.

Table 1: Summary of bleed-hole geometry and arrangement.

Case No.	Mach No.	Incident Shock?	Hole Arrangement	Hole Angle	Hole Diameter
1	2.46	no		90°	0.635 cm (0.25 in)
2	2.46	no		20°	0.635 cm (0.25 in)
3	1.6	no		90°	0.508 cm (0.2 in)
4	1.6	yes		90°	0.508 cm (0.2 in)
5	1.6	yes		90°	0.508 cm (0.2 in)
6	1.6	yes	 shock incident	90°	0.508 cm (0.2 in)

Chapter 3

GOVERNING EQUATIONS

The supersonic flow over the flat is modeled by the ensemble-averaged conservation equations of mass (continuity), momentum (compressible Navier-Stokes), and total energy for a thermally and calorically perfect gas with Sutherland's model for thermal conductivity. The continuity equation is

$$\frac{\partial \rho}{\partial t} + \frac{\partial \rho u}{\partial x} + \frac{\partial \rho v}{\partial y} + \frac{\partial \rho w}{\partial z} = 0 \quad (1)$$

where u , v , and w are the x -, y -, and z -components of the velocity relative to the plate or inlet and the $+x$ direction is the primary flow direction. The momentum equations are

$$\begin{aligned} \frac{\partial}{\partial t} \begin{bmatrix} \rho u \\ \rho v \\ \rho w \end{bmatrix} + \frac{\partial}{\partial x} \begin{bmatrix} \rho u u \\ \rho v u \\ \rho w u \end{bmatrix} + \frac{\partial}{\partial y} \begin{bmatrix} \rho u v \\ \rho v v \\ \rho w v \end{bmatrix} + \frac{\partial}{\partial z} \begin{bmatrix} \rho u w \\ \rho v w \\ \rho w w \end{bmatrix} \\ = \frac{\partial}{\partial x} \begin{bmatrix} P^* + \tau_{xx} \\ \tau_{yx} \\ \tau_{zx} \end{bmatrix} + \frac{\partial}{\partial y} \begin{bmatrix} \tau_{xy} \\ P^* + \tau_{yy} \\ \tau_{zy} \end{bmatrix} + \frac{\partial}{\partial z} \begin{bmatrix} \tau_{xz} \\ \tau_{yz} \\ P^* + \tau_{zz} \end{bmatrix} \end{aligned} \quad (2a)$$

where

$$P^* = P + \frac{2}{3} \rho k \quad (2b)$$

The energy equation is given by

$$\frac{\partial \hat{e}}{\partial t} + \frac{\partial}{\partial x} \left(\hat{e} + P^* \right) u + \frac{\partial}{\partial y} \left(\hat{e} + P^* \right) v + \frac{\partial}{\partial z} \left(\hat{e} + P^* \right) w =$$

$$\begin{aligned} & \frac{\partial}{\partial x} (\tau_{xx} u + \tau_{xy} v + \tau_{xz} w - q_x) + \frac{\partial}{\partial y} (\tau_{yx} u + \tau_{yy} v + \tau_{yz} w - q_y) + \\ & \frac{\partial}{\partial z} (\tau_{zx} u + \tau_{zy} v + \tau_{zz} w - q_z) \end{aligned} \quad (3a)$$

where \hat{e} is mechanical plus thermal energy per unit volume; q_i is Fourier conduction in the i -th direction; and τ_{ij} is the combined laminar and turbulent shear stress.

For the flow above the flat plate, the ensemble-averaged conservation equations given by Eqs. (1) to (3) were closed by the SST turbulence model of Menter^{18,19} which can account for near wall low-Reynolds number effects. The SST model was selected for the flow above the flat plate because it eliminates dependence on freestream turbulence kinetic energy, k , and has a limiter to control overshoot in k with adverse pressure gradients so that separation is predicted more accurately. By using a low-Reynolds number turbulence model, the integration of the conservation equations, as well as the turbulence model, is made all the way to the wall.

The k and ω transport equations in the SST model are as follows:

$$\begin{aligned} & \frac{\partial k}{\partial t} + u \frac{\partial k}{\partial x} + v \frac{\partial k}{\partial y} + w \frac{\partial k}{\partial z} = \frac{P_k}{\rho} - \beta_k k \omega \\ & + \frac{1}{\rho} \left[\frac{\partial}{\partial x} \left(\mu + \frac{\mu_t}{\sigma_k} \right) \frac{\partial k}{\partial x} + \frac{\partial}{\partial y} \left(\mu + \frac{\mu_t}{\sigma_k} \right) \frac{\partial k}{\partial y} + \frac{\partial}{\partial z} \left(\mu + \frac{\mu_t}{\sigma_k} \right) \frac{\partial k}{\partial z} \right] \end{aligned} \quad (4a)$$

$$\frac{\partial \omega}{\partial t} + u \frac{\partial \omega}{\partial x} + v \frac{\partial \omega}{\partial y} + w \frac{\partial \omega}{\partial z} = \frac{P_\omega}{\rho} - \beta_\omega \omega^2 + 2(1-F) \frac{\sigma_2}{\omega} \left(\frac{\partial k}{\partial x} \frac{\partial \omega}{\partial x} + \frac{\partial k}{\partial y} \frac{\partial \omega}{\partial y} + \frac{\partial k}{\partial z} \frac{\partial \omega}{\partial z} \right)$$

$$+\frac{1}{\rho}\left[\frac{\partial}{\partial x}\left(\mu+\frac{\mu_t}{\sigma_\omega}\right)\frac{\partial\omega}{\partial x}+\frac{\partial}{\partial y}\left(\mu+\frac{\mu_t}{\sigma_\omega}\right)\frac{\partial\omega}{\partial y}+\frac{\partial}{\partial z}\left(\mu+\frac{\mu_t}{\sigma_\omega}\right)\frac{\partial\omega}{\partial z}\right] \quad (4b)$$

The first term on the right-hand side (RHS) of the above two equations represents production. The second term on the RHS of Eq. (4a) and the second and third terms in Eq. (4b) represent dissipation and the remaining terms on the RHS represent diffusion. The convective transport terms are all on the left-hand side. In Eqs. (4a) and (4b), the turbulent viscosity production terms, f , and F are given by

$$\mu_t = \min\left(\frac{\rho k}{\omega}, \frac{a_1 \rho k}{\Omega f}\right) \quad (4c)$$

$$P_k = \mu_t \Omega^2 \quad P_\omega = g \rho \Omega^2 \quad (4d,e)$$

$$f = \tanh(\Pi) \quad \Pi = \max(2\Gamma_3, \Gamma_1) \quad (4f,g)$$

$$F = \tanh(\Gamma^4) \quad \Gamma = \min(\max(\Gamma_1, \Gamma_2), \Gamma_3) \quad (4h,i)$$

$$\Gamma_1 = \frac{500\mu}{\xi^2 \rho \Omega} \quad \Gamma_2 = \frac{4\rho \sigma_2 k}{\xi^2 C_\sigma} \quad \Gamma_3 = \frac{\sqrt{k}}{\xi C_\mu \omega} \quad (4j,k,l)$$

$$C_\sigma = \max\left[\frac{2\rho \sigma_2}{\omega}\left(\frac{\partial k}{\partial x}\frac{\partial \omega}{\partial x} + \frac{\partial k}{\partial y}\frac{\partial \omega}{\partial y} + \frac{\partial k}{\partial z}\frac{\partial \omega}{\partial z}\right), 10^{-20}\right] \quad (4m)$$

where Ω is vorticity, and ξ is the normal distance from the solid wall. The constants in Eqs. (4a) to (4e) are calculated by the following weighted formula:

$$\varphi = F\varphi_1 + (1-F)\varphi_2 \quad (4n)$$

In the above equation, φ is a constant such as σ_k , σ_ω , β_k , and g that is being sought by a weighted average between φ_1 and φ_2 . The φ_1 and φ_2 terms corresponding to constant such as σ_k , σ_ω , β_k , g_1 , and g_2 are as follows:

$$\sigma_{k1} = 0.85 \quad \sigma_{k2} = 1.0 \quad (4o,p)$$

$$\sigma_{\omega 1} = 0.5 \quad \sigma_{\omega 2} = 0.856 \quad (4q,r)$$

$$\beta_{k1} = 0.075 \quad \beta_{k2} = 0.0828 \quad (4s,t)$$

$$g_1 = \frac{\beta_{k1}}{C_\mu} - \frac{\sigma_1 \theta^2}{\sqrt{C_\mu}} \quad g_2 = \frac{\beta_{k2}}{C_\mu} - \frac{\sigma_2 \theta^2}{\sqrt{C_\mu}} \quad (4u,v)$$

Other constants, which do not involve weighted averaging, are $\theta = 0.41$, $\beta_\omega = C_\mu = 0.09$, and $a_1 = 0.31$.

The boundary conditions used for the turbulence model (k - ω with Menter's SST) are as follows. On the wall, the turbulent kinetic energy (k) was set to zero and the dissipation rate per unit of turbulent kinetic energy (ω) was set equal to $60\nu/(\beta\Delta y)$. With this boundary condition, β equals $3/40$ and Δy is the normal distance of the first grid point from the wall. With this model, the first grid point from the wall was required to be within a y^+ of unity. At all other boundaries, k and ω were extrapolated.

Since the focus of this research is on the development of bleed boundary conditions, the boundary conditions for the governing equations are included with the bleed boundary conditions in a separate chapter (Chapter 4).

Chapter 4

BOUNDARY CONDITION FORMULATION

In Chapter 3, the conservation equations governing the problem are described. Typically, the boundary conditions for the entire problem are included in the chapter describing the governing equations. In this thesis, however, this general standard of practice is not being followed since the focus of the research has been on the development of bleed boundary conditions. All of the boundary conditions employed in the simulations of the flow above the flat plate will be described in this chapter.

For the simulations that resolved the flow above the flat plate, though the holes, and in the plenum, the boundary conditions used are as follows (Figure 2, Chapter 2). At the inflow boundary above the flat plate, all flow variables were specified at the freestream condition except those in the region containing the boundary layer. In the boundary layer, the compressible, turbulent boundary layer profile of Huang, et al.²⁰ was employed. At locations where an incident shock crossed a boundary, pre- and post-oblique shock conditions based on inviscid theory were imposed. At the freestream boundary, all flow variables were specified at the freestream conditions. At the outflow boundary, all flow variables were extrapolated. At the symmetry boundaries, zero derivatives of the dependent variables were imposed and the velocity component normal to the symmetry boundary was set equal to zero. At the exit of the plenum, a back pressure (P_b) was imposed and the density and velocity were extrapolated. Finally, all of the solid surfaces were treated as no-slip, adiabatic walls and a zero normal pressure gradient was imposed.

For the simulations that only resolved the flow above the flat plate, the boundary conditions used at the inflow, outflow, freestream, symmetry and solid boundaries are the same as those just described. At each hole location on the surface of the plate, one of the developed bleed boundary conditions was imposed and the derivatives of all of the primary flow variables were set to zero.

In this study, four bleed boundary conditions were developed and evaluated for the different cases. All five of the bleed boundary conditions were at first analyzed for applicability and then only two (Cd_BC and DNS_BC) were chosen for further analysis. They are as follows:

1) DNS_BC (Direct Numerical Simulation Boundary Condition)

The normal velocity at each point within a hole is taken from the simulations that resolved the flow through the holes and the plenum. The density, pressure and two remaining velocity components at these points are extrapolated from the flow above the plate by assuming zero normal derivatives. The total energy is then computed from this information using the equation of state.

2) Cd_BC (Discharge Coefficient Boundary Condition)

The normal velocity, W , is calculated using a discharge coefficient (C_D), constant over each individual hole, where

$$W = C_D \times \sqrt{\frac{\gamma P}{\rho}} \quad (5)$$

The discharge coefficient was determined for a given configuration by calculating the value of C_D for each grid point within a hole from the DNS results. A density-weighted average of these values was used to determine the applied value of C_D . The density, pressure and two remaining velocity components at the hole points are extrapolated from

the flow above the plate by assuming zero normal derivatives. The total energy is then computed from this information using the equation of state.

3) W_Avg (Average Normal Velocity Boundary Condition)

The normal velocity is constant over each hole and the numerical value of the average normal velocity is determined from density-weighted averaging of the DNS results. The density, pressure and two remaining velocity components at the hole points are extrapolated from the flow above the plate by assuming zero normal derivatives. The total energy is then computed from this information using the equation of state.

4) W_Profile (Normal Velocity Profile Boundary Condition)

Each hole is divided in to two segments: one region consisting of 90% of the hole (upstream) and the other only 10% of the hole area (downstream). The normal velocity profile is constant and negative over each segment and the numerical value of the average normal velocity for that segment is determined from density-weighted averaging of the DNS results. The density, pressure and two remaining velocity components at the hole points are extrapolated from the flow above the plate by assuming zero normal derivatives. The total energy is then computed from this information using the equation of state.

Each of these boundary conditions was chosen for study for a particular reason. The DNS_BC was chosen to allow for an examination of the importance of the normal velocity distribution in the hole. The W_Avg boundary condition was chosen to investigate the effects of neglecting the spatial variations in the normal velocity distribution. The Cd_BC boundary condition is the most useful of the developed boundary conditions. In the future, it is anticipated that, using information only about

the bleed rate needed, a model will be developed that can tune the discharge coefficient so that it can model the flow through the holes. Finally, the W_Profile boundary condition was intended to model the “barrier” shock inside the bleed hole.

In this series of simulations, the Cd_BC boundary condition was implemented in two ways. In the first, the Cd_BC was applied only on the portions of the plate where the bleed holes are located (denoted as cases (c) and (d) in Table 4, Chapter 6). This application of Cd_BC accounts for the individual bleed holes and their arrangement on the plate. The second method of implementing the Cd_BC boundary condition applied the discharge coefficient over the entire bleed region: treating the entire bleed region as a porous wall or slot instead of as a sequence of individual holes. The porous wall application of Cd_BC is referred to as Cd_BC-slot (denoted as cases (e) in Table 4, Chapter 6). The value of the discharge coefficient applied in the slot cases was identical to the discharge coefficient used in the Cd_BC cases, with a correction being made to account for the porosity of the slot.

Chapter 5

NUMERICAL METHOD OF SOLUTION

Solutions to the governing equations were obtained by using a cell-centered, finite volume code called CFL3D (Thomas, et al.²¹ and Rumsey & Vatsa²²). In this code, all inviscid terms were approximated by the third-order accurate flux-difference splitting of Roe^{23,24} with the slope limiter of Chakavarthy and Osher²⁵. All diffusion terms were approximated conservatively by differencing derivatives at cell faces and the spatial differences for the Euler fluxes utilized a third-order, upwind scheme. Since only steady-state solutions were of interest, the time derivatives were approximated by the Euler implicit formula. The system of nonlinear equations that resulted was analyzed using a diagonalized alternating-direction scheme²⁶ with local time stepping (local Courant number is fixed at unity) and a three-level V-cycle multigrid^{27,28}.

For simulations that resolved the flow through the bleed holes and the plenum, a multi-block grid system involving patched and overlapped grids were used. Above the plate, an H-H grid is used. This grid has grid points clustered next to the plate to resolve the boundary-layer flow there with the first grid point away from the plate having a y^+ less than unity and at least five points within a y^+ of 5. These stringent requirements on grid resolution near the wall are stipulated by the SST turbulence model. When there are incident and reflected shock waves above the plate, the H-H grid is solution adapted to resolve the sharp gradients associated with the shock waves. An H-H grid was also used in the plenum. For each bleed hole, two grids are used, an O-H grid to get the geometry of the hole correctly and an H-H grid to remove the centerline singularity associated with

the O-H grid. The grids in each of the bleed holes were overlapped. The overlapped grids in the bleed holes were patched to the grids above the plate and in the plenum.

For the simulations that employed bleed boundary conditions instead of resolving the flow through the holes and in the plenum, only the H-H grids above the plate were used. Table 2 summarizes the number of grid points used for each of the cases simulated. Note that two H-H grids were used for each case, one fine and one coarse. The fine H-H grid is identical to the one used above the plate in simulations that resolved the flow in the holes and plenum. The coarse H-H has only one grid point in the normal holes and two grid points in the inclined holes. By not resolving the holes and the plenum (fine H-H grid), the number of grid points needed can be reduced by a factor of about two when compared to cases that do require holes and plenums to be resolved. By using only one or two grid points in each hole, the number of grid points needed is reduced by a factor of about 250-350 (Table 2). Figures 7 and 8 show a typical fine and coarse H-H grid. A grid independence study was not performed for the fine-mesh cases because it was conducted for the flow through the holes and in the plenum in Reference 7.

In this study, only steady-state solutions were of interest. A solution is said to be converged if the second-norm of the residual drops at least three orders of magnitude and the predicted Mach number and pressure profiles downstream of the bleed region do not change.

Table 2: Grid dimensions and total number of grid points for the cases studied.

Case No.	Fine Grid	Grid Points	Coarse Grid	Grid Points	Reduction Factor*
1	201 x 17x 81 449 x 33 x 49	1,002,810	23 x 3 x 81	5,589	179
2	145 x 17 x 97 321 x 33 x 49	758,162	13 x 3 x 97	3,783	200
3	337 x 29 x 101	987,073	26 x 3 x 101	7,878	125
4	337 x 29 x 101	987,073	26 x 3 x 101	7,878	125
5	337 x 41 x 101	1,395,517	26 x 4 x 101	10,504	133
6	337 x 29 x 101	987,073	26 x 3 x 101	7,878	125

*** Reduction factor is calculated here by comparing the number of grid points used in the coarse grid simulations to the number of grid points used in the fine grid simulations. The grids used for the DNS results were typically twice the size of the fine grids used.**

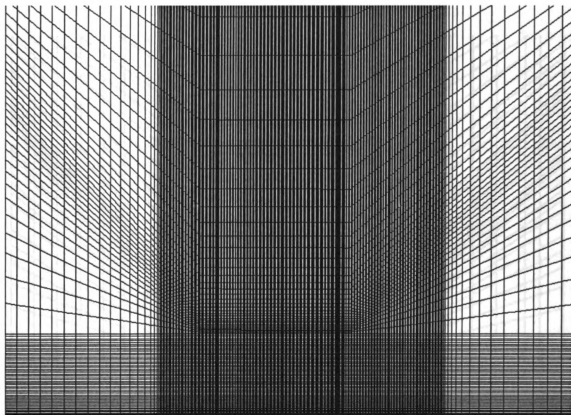
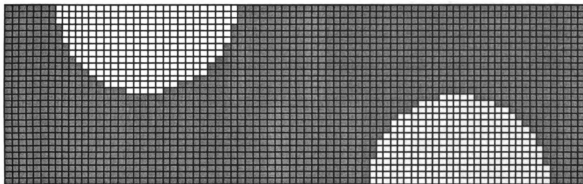


Figure 7: Fine H-H grid above plate, plate surface (top) and side view.
 In the top view, the lighter shade of grey regions represent hole locations.

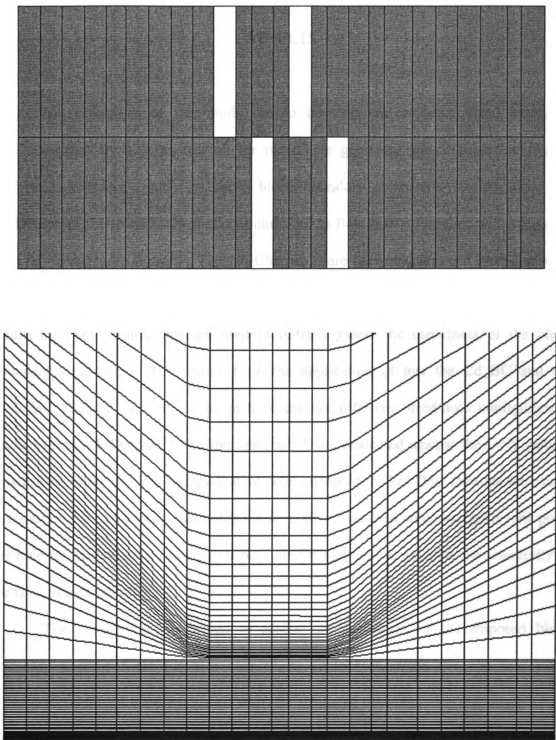


Figure 8: Coarse H-H grid above plate, plate surface (top) and side view. In the top view, the lighter shade of grey regions represent hole locations.

Chapter 6

RESULTS

The objectives of this study are to develop and evaluate bleed boundary conditions that are able to account for bleed-hole geometry and arrangement and to perform a sensitivity study on those bleed boundary conditions. Results from the application of the four bleed boundary conditions to flow over a flat plate with staggered rows of normal holes (Case #1, Table 2, Chapter 3) are presented first and compared with simulations that resolved the flow through the holes and the plenum (referred to as ‘DNS results’). These simulations are used to initially assess the usefulness of the bleed boundary conditions. The results from the application of just the Cd_BC and the DNS_BC boundary conditions to each of the six different bleed-hole configurations studied (Table 2, Chapter 3) are then presented and evaluated against the DNS results. Downstream flow profiles and qualitative assessments of the key flow features were used as measures for comparison. Simulations were also conducted on coarse grids (one point per hole for normal holes, two points per hole for inclined) to examine the sensitivity of the flow to mesh density.

The simulations performed to assess the usefulness of the imposed bleed boundary conditions are listed as case #1 of Table 1 (Chapter 2). The four bleed boundary conditions were compared with the results of the simulation that resolved the flow through both the normal holes and the plenum (DNS results) for supersonic flow over a flat plate without the presence of an embedded shock ($M_{\infty} = 2.46$).

Figure 9 shows the baseline, DNS results, for the pressure contours in the left symmetry plane and on the surface of the plate. It also shows velocity vectors at 10^{-5} m above the plate. The direction of the freestream flow is from left to right in the diagram. In this figure, the structure of the “barrier” shock formed within and about each hole can be seen. The velocity vectors clearly demonstrate that the “barrier” shocks do not cause flow separation downstream of the holes. This simulation serves as a reference (and is listed as such in Figures 12-16) for evaluating all of the other bleed boundary conditions that were examined in the first part of the study.

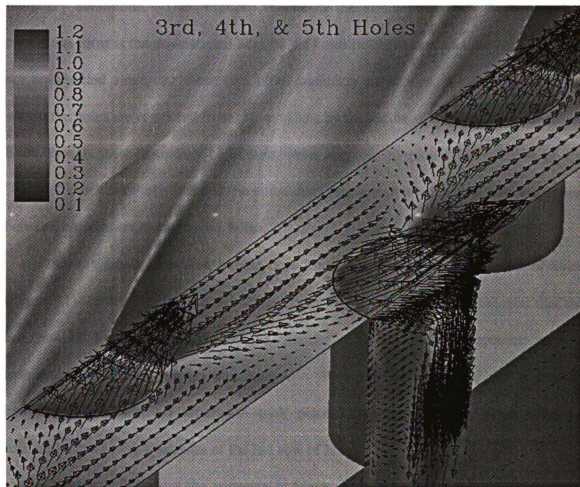


Figure 9: DNS results for pressure contours in left symmetry plane and on plate surface with velocity vectors at $z = 10^{-5}$ m above the plate.

Figure 10 shows the pressure contours above the plate for the simulations that resolved the flow through the holes and plenum (DNS result) and the four bleed boundary conditions that were assessed in this part of the study. The left symmetry plane and the plate surface were chosen for plotting: the same scale is used in each plot. From the figure, it can be seen that all of the bleed boundary conditions that were developed correctly produce some of the qualitative features of the flow field. Most importantly, each of the imposed bleed boundary conditions reproduced the formation of the “barrier” shock. A significant difference, however, is observed for the W_Avg and Cd_BC boundary conditions. The “barrier” shocks in the simulations with these boundary conditions form at the downstream edge of the holes rather than within the holes. This is not unexpected since, for these two bleed boundary conditions, the normal velocities within the holes are restricted to negative values by the nature of the boundary condition. Even though these boundary conditions were not able to model the location of the “barrier” shock correctly, it should be noted that there was no evidence of flow separation between bleed holes in successive holes.

A very small separation bubble does form downstream of the last row of holes (Figure 11) for the W_Avg and the Cd_BC boundary conditions. This indicates that the last row of holes downstream of the “barrier” shock plays an important role in accelerating the flow through the “barrier”. With the DNS_BC and the W_Profile boundary conditions, no separation took place either between the bleed holes in successive rows or downstream of the last row of holes.

Figures 12-14 show the variation in Mach number, pressure and normal velocity across the middle of the third row holes. The figures show that all of the bleed boundary

DNS results



DNS_BC



W_Avg



Cd_BC



W_Profile

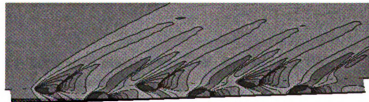


Figure 10: Pressure contours in left symmetry plane and on plate surface for different bleed BCs.
The same scale is used for each of the plots.

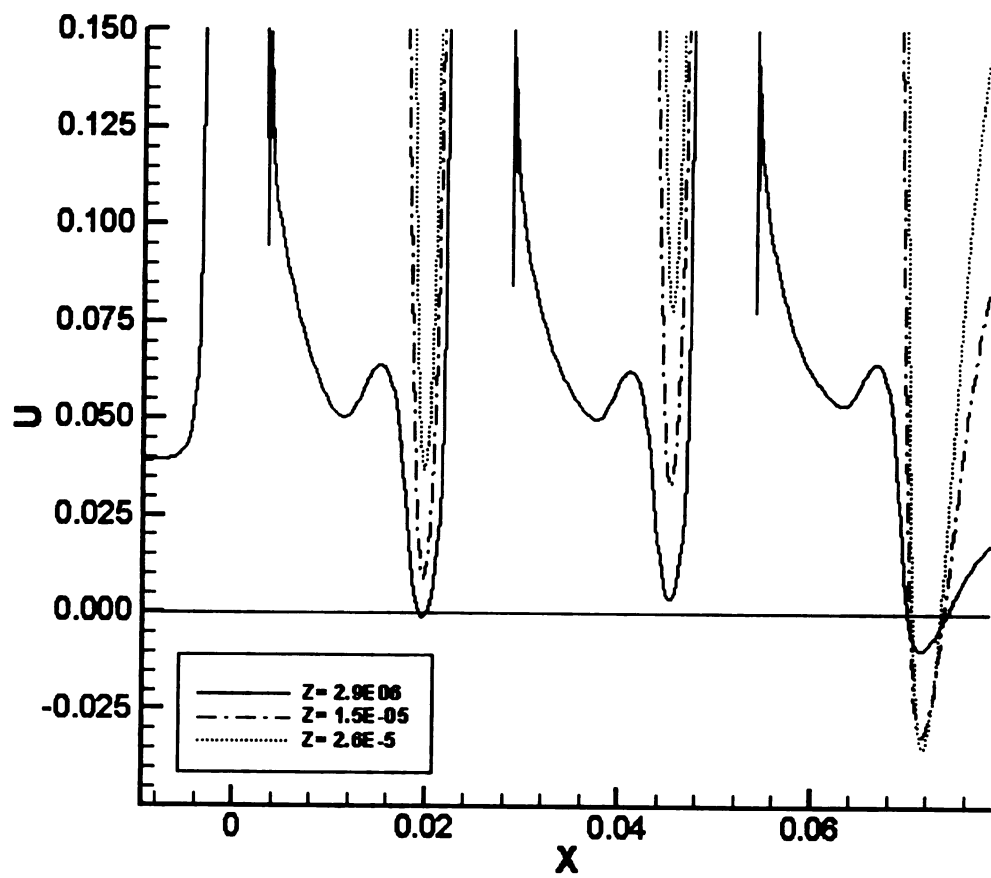


Figure 11: Separation downstream – W_{Avg} and Cd_{BC} boundary conditions.

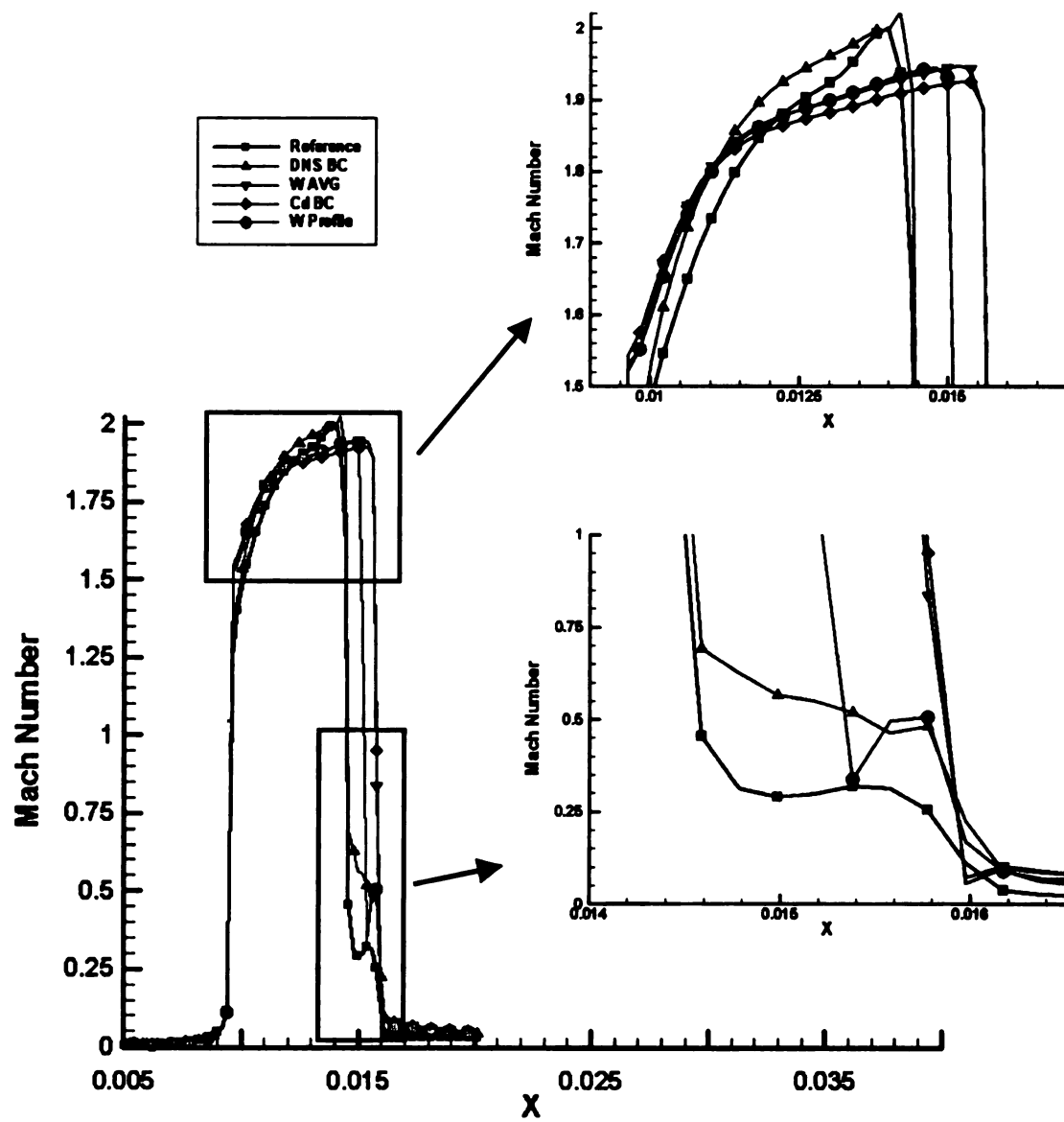


Figure 12: Mach number profile across third row of normal holes.

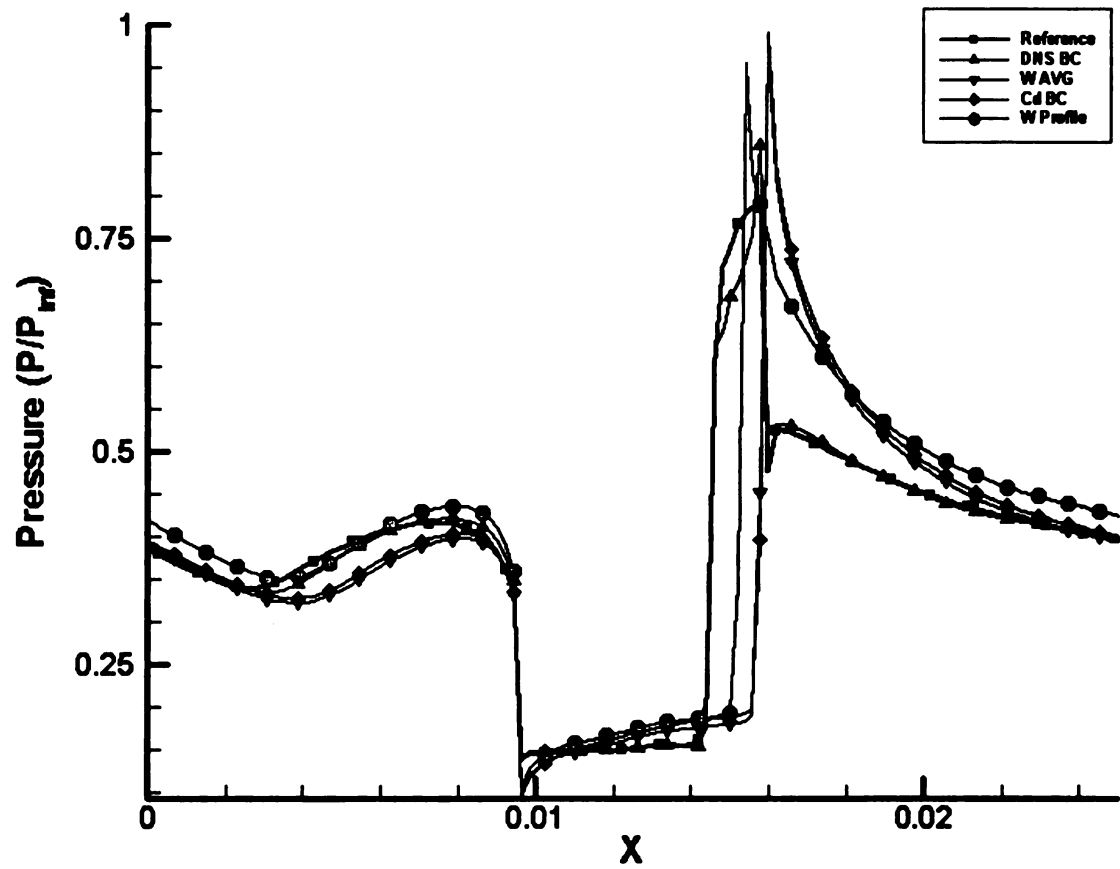


Figure 13: Normalized pressure profile across third row of normal holes.

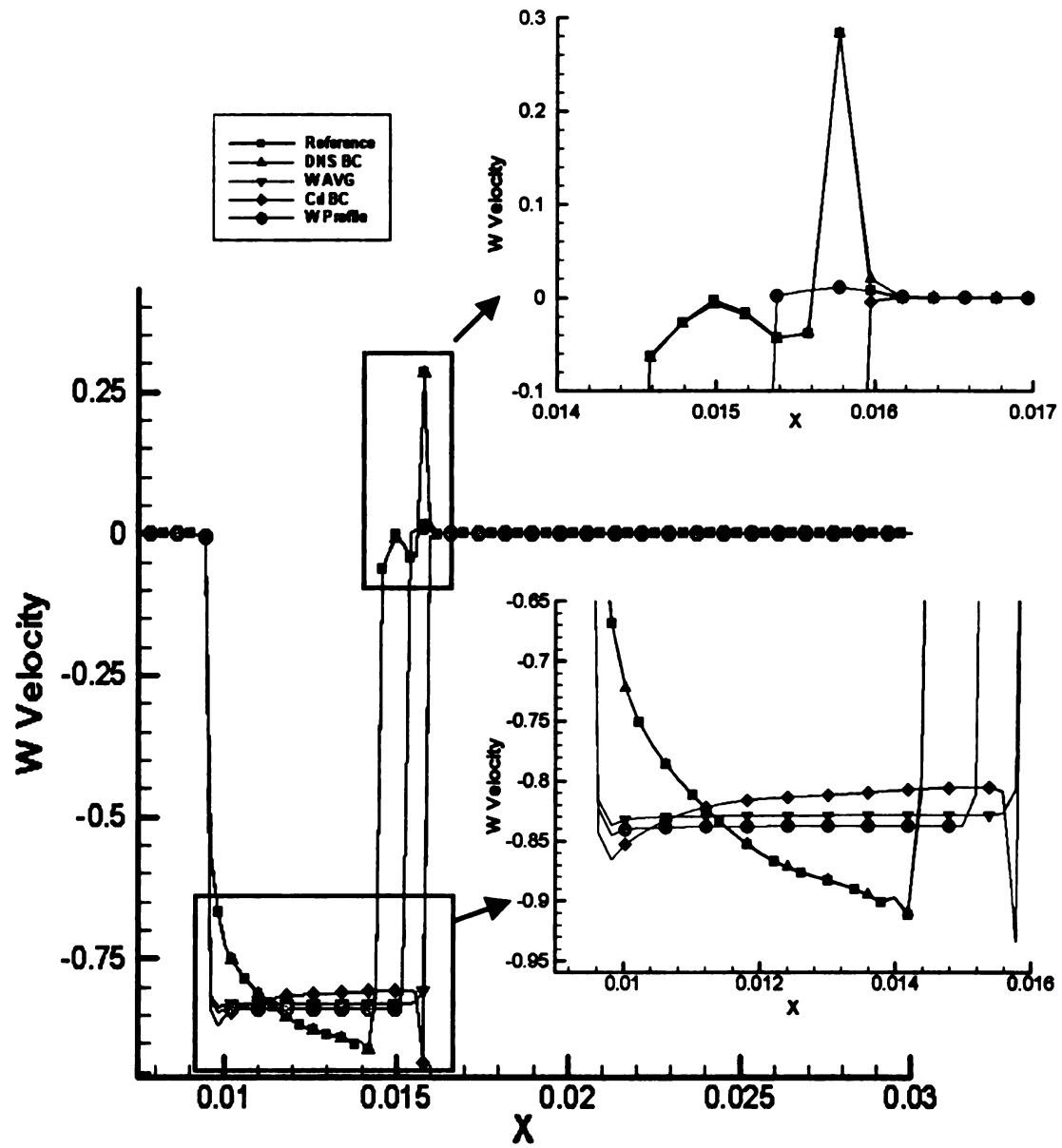


Figure 14: Normal velocity (W) profile across third row of normal holes.

conditions perform reasonably well when compared with the DNS results. The greatest discrepancies occur here for the simplest of the imposed boundary conditions: Cd_BC and W_Avg. Once again, these discrepancies occur in the structure of the “barrier” shock because the nature of these boundary conditions permits flow in only one direction: forcing the location of the “barrier” shock to the terminal/downstream side/edge of the hole.

Figures 15 and 16 show the Mach number and pressure profiles near the plate at streamwise distances of two hole diameters (2D) before and one hole diameter (1D) after the bleed region. Compared with the DNS results, all of the bleed boundary conditions were able to predict the downstream Mach number profile with considerable accuracy. In the Mach number profiles, it is observed that the profiles downstream of the bleed region are considerably fuller for each of the bleed boundary conditions applied. The pressure profiles downstream of the bleed region are also reasonable when compared with the DNS results.

The final figures for this segment of the research (Figure 17 and Figure 18) show the results obtained for the coarse case using only the W_Avg boundary condition. Despite the fact that the coarse grid system contains only 5,589 grid points (compared to fine grid system's 1.003×10^6 grid points) the coarse solution performs quite well. The coarse grid is the coarsest that can be used and still model the normal holes as individual entities: only one grid point per bleed hole. This level of coarsening corresponds to a significant reduction in the number of grid points between the simulations that only resolved the flow above the plate (which was already a simplification) and the coarse grid.

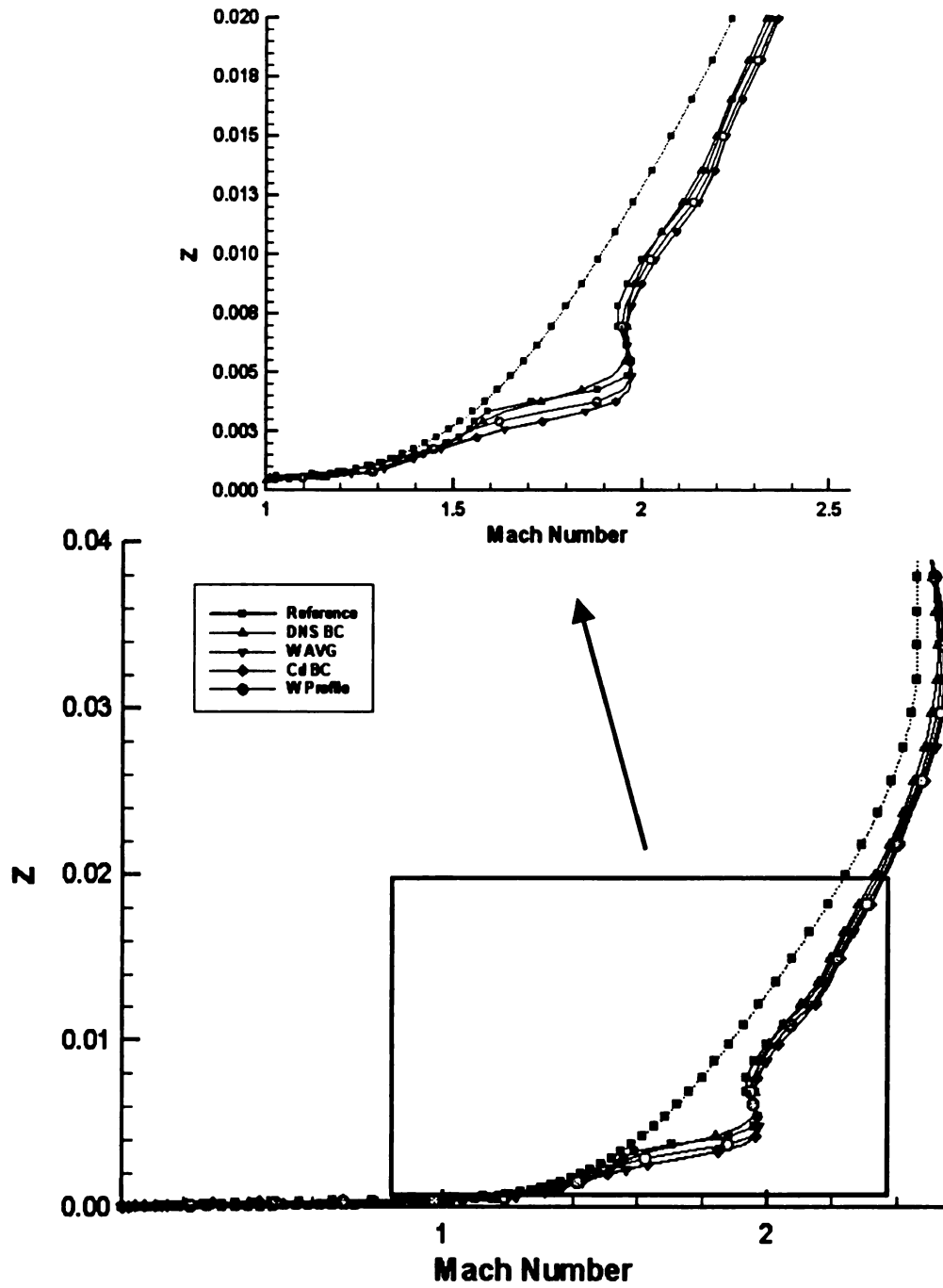


Figure 15: Mach number profile 1D downstream of last row of holes.

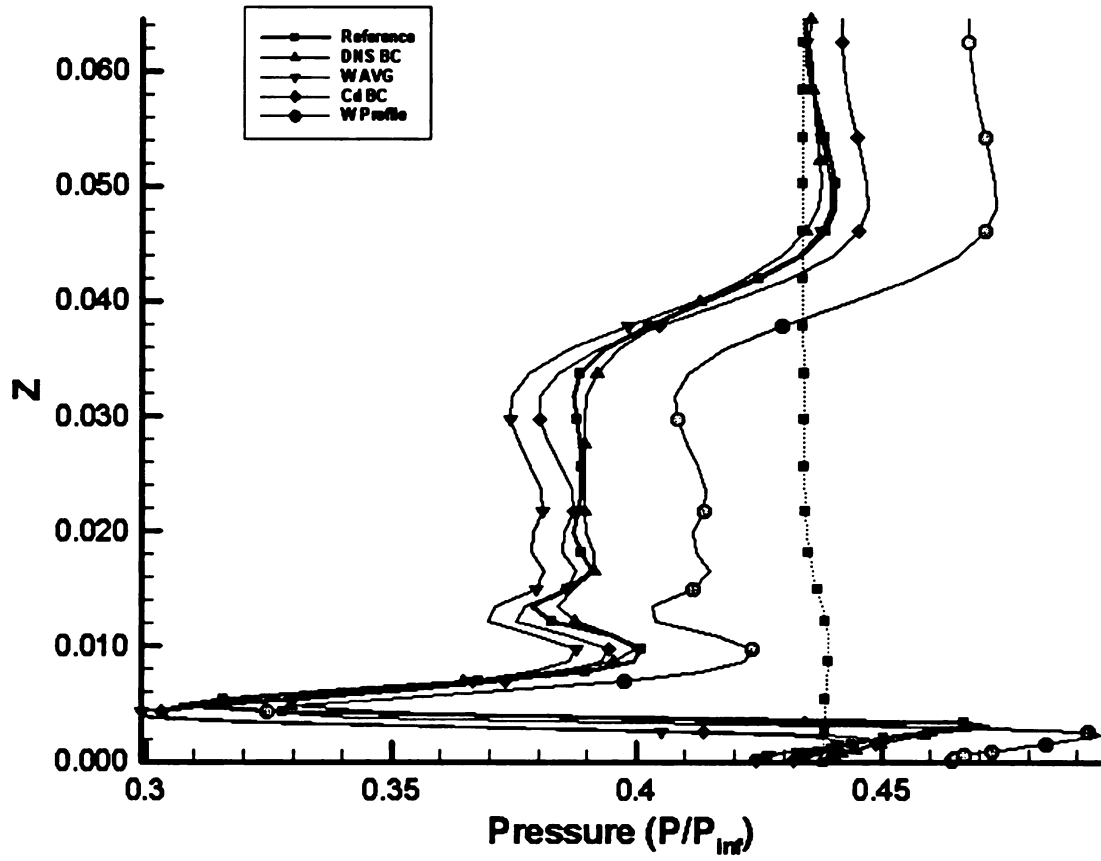


Figure 16: Normalized pressure profile 1D downstream of last row of holes.

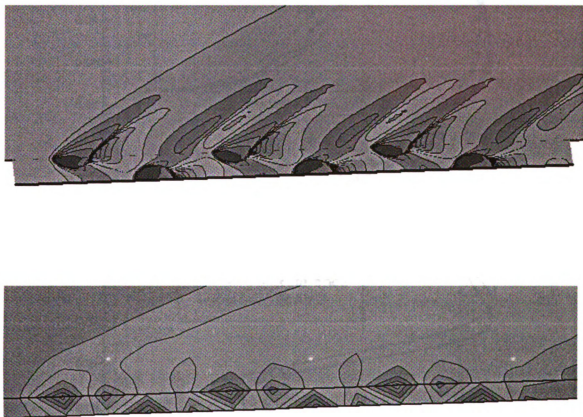


Figure 17: Contour plots of pressure for the DNS results (upper) and coarse grid case (lower).

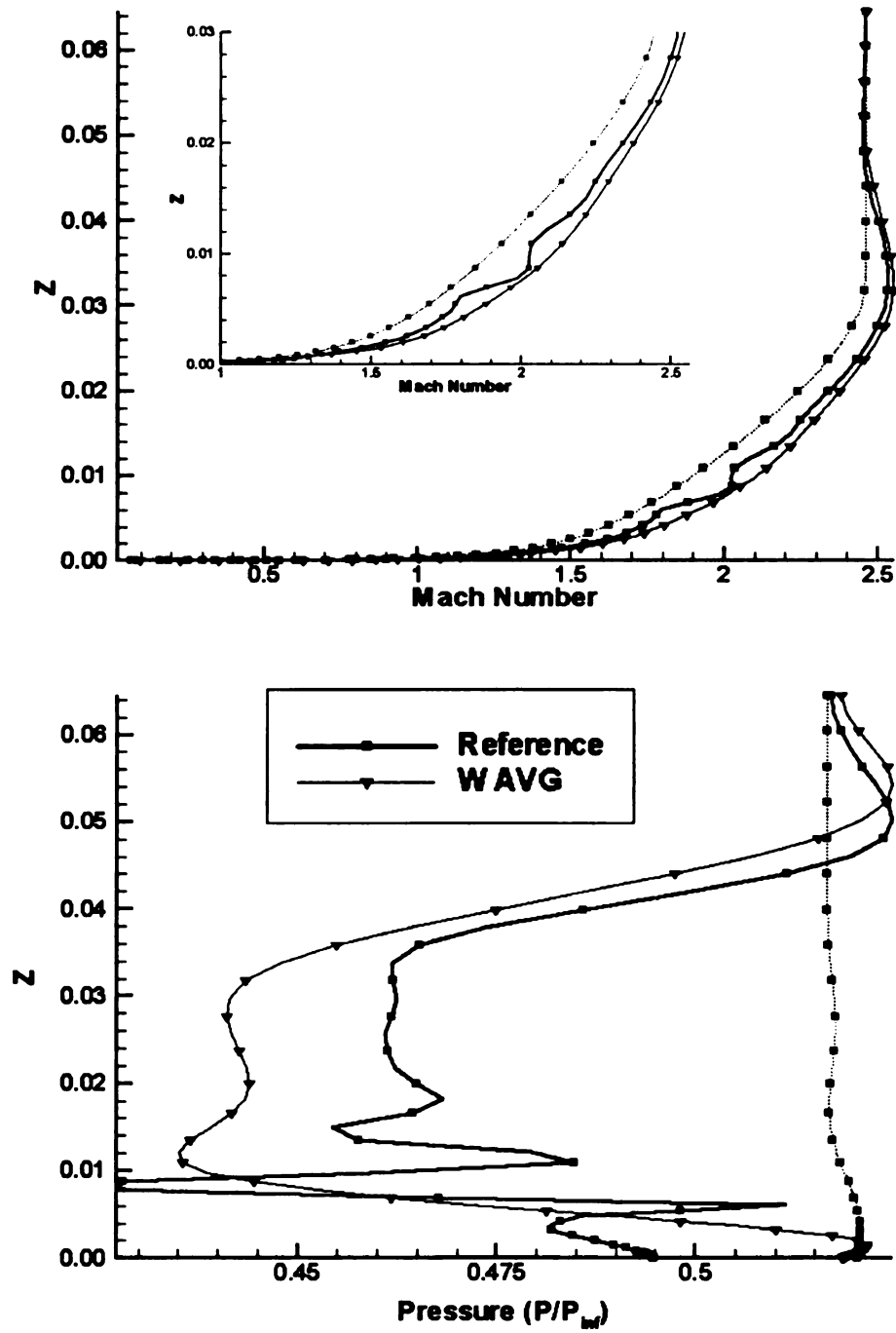


Figure 18: Pressure and Mach number profiles 1D downstream of last row of holes – coarse case.

Figure 17 shows qualitatively the pressure contours in the left symmetry plane and on the first plane above the plate (10^{-5} m). From this figure it can be seen that even with one grid point per hole, the “barrier” shocks are still predicted, however, their strength is considerably weakened and their location is smeared.

Figure 18 shows the Mach number and pressure profiles near the plate for the coarse case at streamwise distances of two hole diameters (2D) before and one hole diameter (1D) after the bleed region. The Mach number profile for the coarse application of the W_Avg boundary condition does not match the DNS results as well as the previous level of resolution, however, considering the degree of coarsening that has occurred, the results are quite good.

The results from the simulations that were designed to assess the applicability of the hole boundary conditions show the bleed boundary conditions capable of faithfully reproducing the downstream profiles as well as capturing the central flow features of the bleed process. Two of the bleed boundary conditions, DNS_BC and Cd_BC, were then evaluated against the DNS results for six different bleed-hole configurations (Table 3). Simulations were also conducted to assess the effects of mesh density. The DNS results (cases denoted by (a)) serve as the reference or baseline against which the accuracy of all other cases is evaluated. The DNS results are also used to provide the normal velocity needed by the DNS_BC and the discharge coefficient needed by the Cd_BC boundary condition.

Table 4 summarizes the bleed flow rate through each hole, the effective discharge coefficient for each hole, and the average discharge coefficient for each configuration. The data in this table are all computed from the DNS results. From this table, it can be

seen that the discharge coefficient does not vary appreciably from hole to hole ($< 4\%$, except for cases 2 and 6). Despite the fact that the bleed rates upstream of the incident shock are about half of those downstream of it, the discharge coefficient is relatively unaffected. This is an indication that, in future research, it is reasonable to use the same average discharge coefficient upstream and downstream of the incident shock. The average values given in Table 4 are the ones used in the Cd_BC-slot applications.

Table 3: Bleed-boundary conditions applied and mesh refinement

Case No.	Mach No.	Bleed BC	Level of Mesh Refinement
1 (a)	2.46	DNS	fine
(b)		DNS_BC	fine
(c)		Cd_BC	fine
(d)		Cd_BC	coarse
2 (a)	2.46	DNS	fine
(b)		DNS_BC	fine
(c)		Cd_BC	fine
(d)		Cd_BC	coarse
3 (a)	1.6	DNS	fine
(b)		DNS_BC	fine
(c)		Cd_BC	fine
(d)		Cd_BC	coarse
(e)		Cd_BC-slot	coarse
4 (a)	1.6	DNS	fine
(b)		DNS_BC	fine
(c)		Cd_BC	fine
(d)		Cd_BC	coarse
(e)		Cd_BC-slot	coarse
5 (a)	1.6	DNS	fine
(b)		DNS_BC	fine
(c)		Cd_BC	fine
(d)		Cd_BC	coarse
(e)		Cd_BC-slot	coarse
6 (a)	1.6	DNS	fine
(b)		DNS_BC	fine
(c)		Cd_BC	fine
(d)		Cd_BC	coarse
(e)		Cd_BC-slot	coarse

Table 4: Summary of bleed rates and discharge coefficients for each bleed-hole

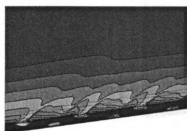
	Case 1	Case 2	Case 3	Case 4	Case 5	Case 6																		
Row 1 Holes																								
m_b (kg/s):	2.42×10^{-8}	6.60×10^{-8}	4.86×10^{-5}	5.17×10^{-5}	5.17×10^{-5}	4.90×10^{-5}																		
C_D :	0.7208	0.4355	0.4492	0.4763	0.4692	0.4580																		
Row 2 Holes																								
m_b (kg/s):	2.44×10^{-8}	6.90×10^{-8}	5.04×10^{-5}	5.54×10^{-5}	5.41×10^{-5}	5.44×10^{-5}																		
C_D :	0.7237	0.4734	0.4569	0.4593	0.4481	0.5084																		
Row 3 Holes																								
m_b (kg/s):	2.53×10^{-8}	7.80×10^{-8}	5.13×10^{-5}	9.36×10^{-5}	10.62×10^{-5}	9.55×10^{-5}																		
C_D :	0.7329	0.5979	0.4597	0.4685	0.4860	0.4776																		
Row 4 Holes																								
m_b (kg/s):	2.54×10^{-8}	7.69×10^{-8}	5.14×10^{-5}	10.01×10^{-5}	11.64×10^{-5}	10.91×10^{-5}																		
C_D :	0.7384	0.5758	0.4604	0.4628	0.4993	0.5481																		
Row 5 Holes																								
m_b (kg/s):	2.54×10^{-8}	8.13×10^{-8}	<table><tr><th colspan="6">Average C_D</th></tr><tr><th>Case 1</th><th>Case 2</th><th>Case 3</th><th>Case 4</th><th>Case 5</th><th>Case 6</th></tr><tr><td>0.7337</td><td>0.5569</td><td>0.4566</td><td>0.4667</td><td>0.4757</td><td>0.4980</td></tr></table>				Average C_D						Case 1	Case 2	Case 3	Case 4	Case 5	Case 6	0.7337	0.5569	0.4566	0.4667	0.4757	0.4980
Average C_D																								
Case 1	Case 2	Case 3	Case 4	Case 5	Case 6																			
0.7337	0.5569	0.4566	0.4667	0.4757	0.4980																			
C_D :	0.7412	0.6512																						
Row 6 Holes																								
m_b (kg/s):	2.54×10^{-8}	7.88×10^{-8}																						
C_D :	0.7450	0.6075																						

Figure 19 shows the Mach number contours obtained by direct numerical simulation (DNS results) for all of the bleed hole arrangements studied in this part of the research. This figure demonstrates that there are considerable differences in the flow field for the different cases investigated. This indicates that the collective set of cases provides a good test of the bleed boundary conditions.

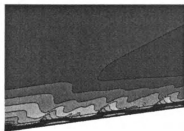
An examination of the performance of the DNS_BC and Cd_BC bleed boundary conditions on the fine grid is displayed in Figures 20 to 24. Figure 20 shows the Mach number contours obtained by using DNS_BC and Cd_BC to be qualitatively similar to those obtained by direct numerical simulation (only case 5 is shown because other cases are similar).

Figures 21 to 24 show a quantitative comparison of the DNS_BC and the Cd_BC boundary conditions with the DNS results. These figures compare in detail the pressure and Mach number distribution along a third-row hole and at 1D downstream of the last-row holes. From these figures, it can be seen that the DNS_BC is better than the Cd_BC, although the Cd_BC is adequate in capturing most of the features, including the “barrier” shock. The greatest discrepancy between the Cd_BC boundary condition and the DNS_BC is in the location of the “barrier” shock within the hole. With the Cd_BC boundary condition, Figures 21 and 22 show that the “barrier” shock is shifted from occurring inside the hole to just outside of the hole. This is also the reason for the shift in the pressure curve on downstream side of the hole. This deficiency, however, is unimportant if the entire hole is to be represented by only one or two grid points.

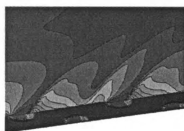
Downstream of the bleed-holes, the Cd_BC and DNS_BC boundary conditions produce nearly identical profiles. Both Mach number profiles follow the general pattern



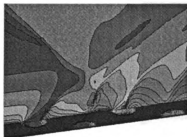
Case #1



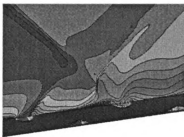
Case #2



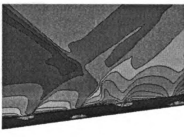
Case #3



Case #4



Case #5



Case #6

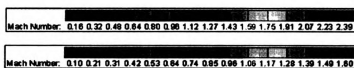
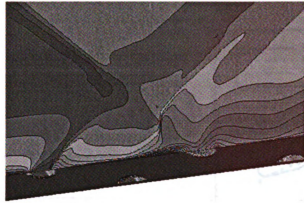
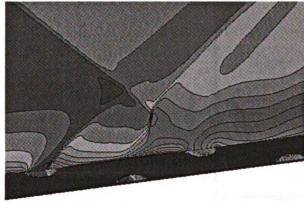


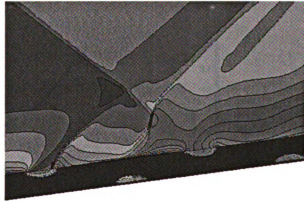
Figure 19: Mach contours in left symmetry plane and on plate surface of the DNS results for all of the cases



DNS Results

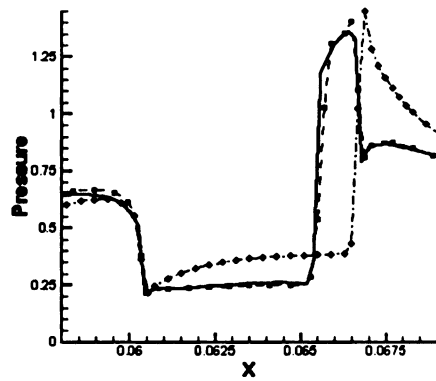


DNS_BC

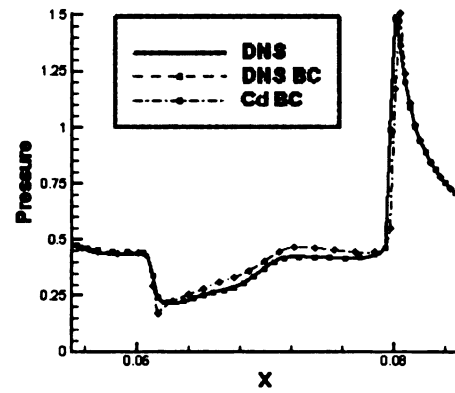


Cd_BC

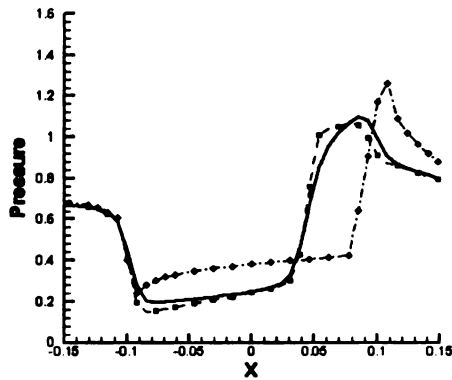
Figure 20: Mach number contours in left symmetry plane ($y = L_y$) and on plate surface ($z = 0$) for Case 5 and DNS, DNS_BC, and Cd_BC. Contour level is the same as B in Fig. 19.



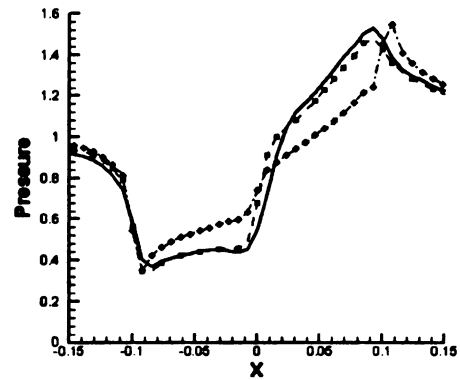
Case #1



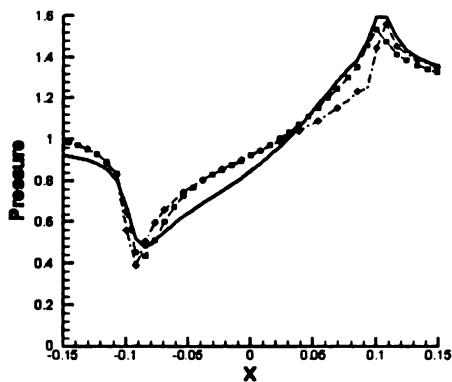
Case #2



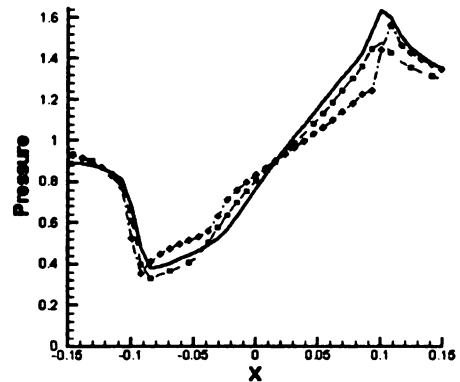
Case #3



Case #4



Case #5



Case #6

Figure 21: Normalized pressure along middle of 3rd row hole at $z = 0$ (plate surface) for DNS, DNS_BC, and Cd_BC.

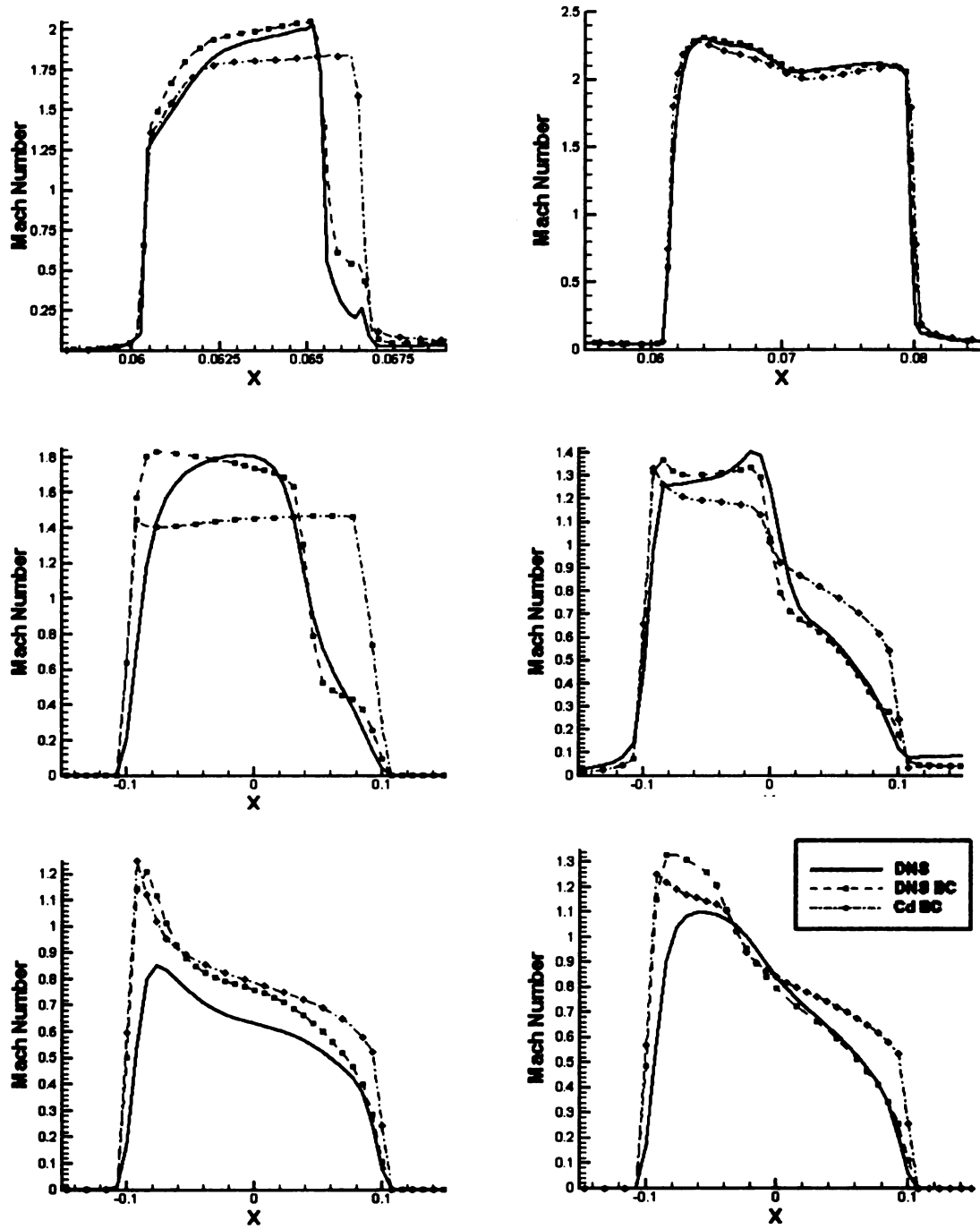


Figure 22: Mach number along middle of 3rd row hole at $z = 0$ (plate surface) for DNS, DNS_BC, and Cd_BC.
Same case order as Figure 22.

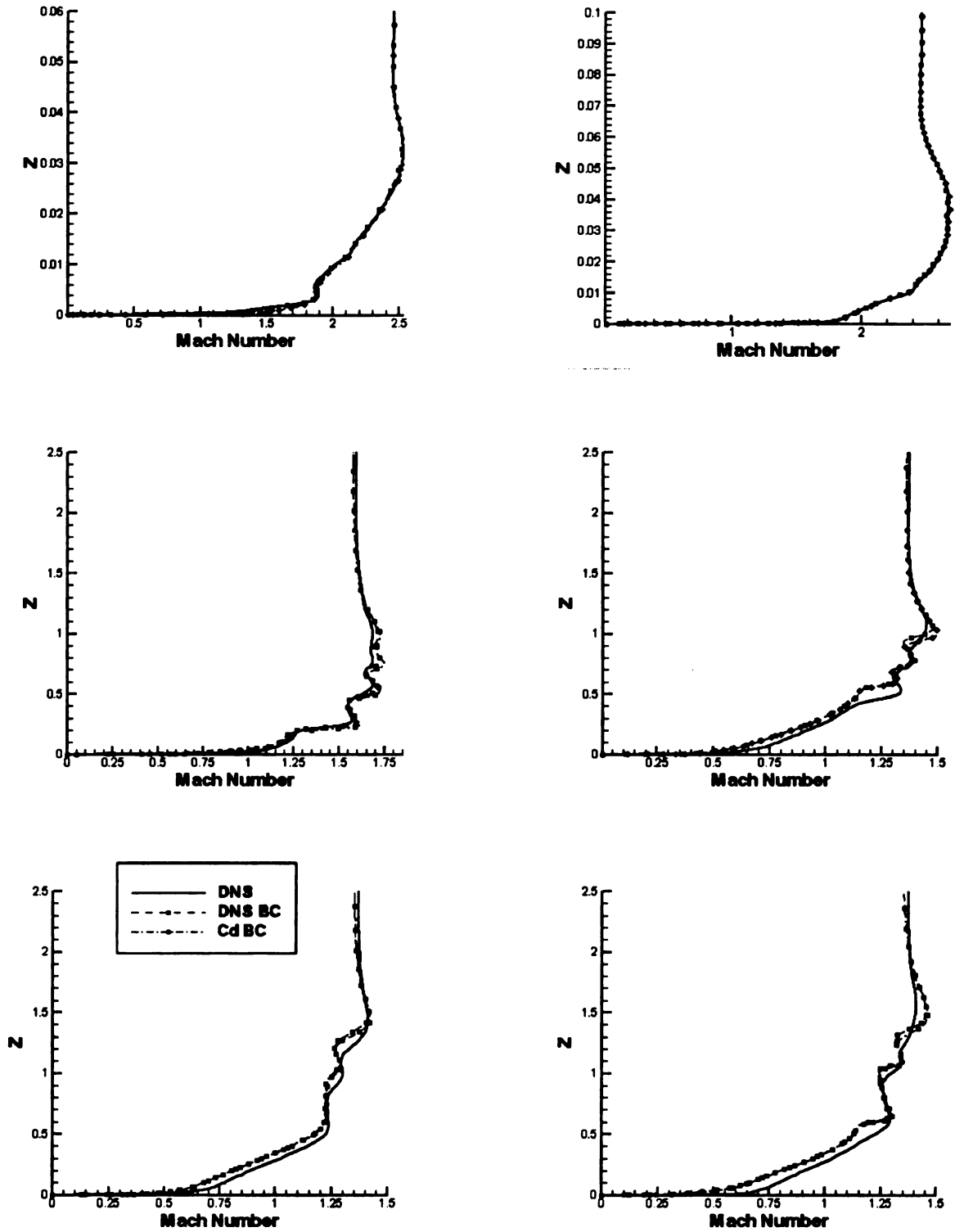


Figure 23: Mach number at 1D downstream of last-row holes for DNS, DNS_BC, and Cd_BC. Same case order as Figure 22.

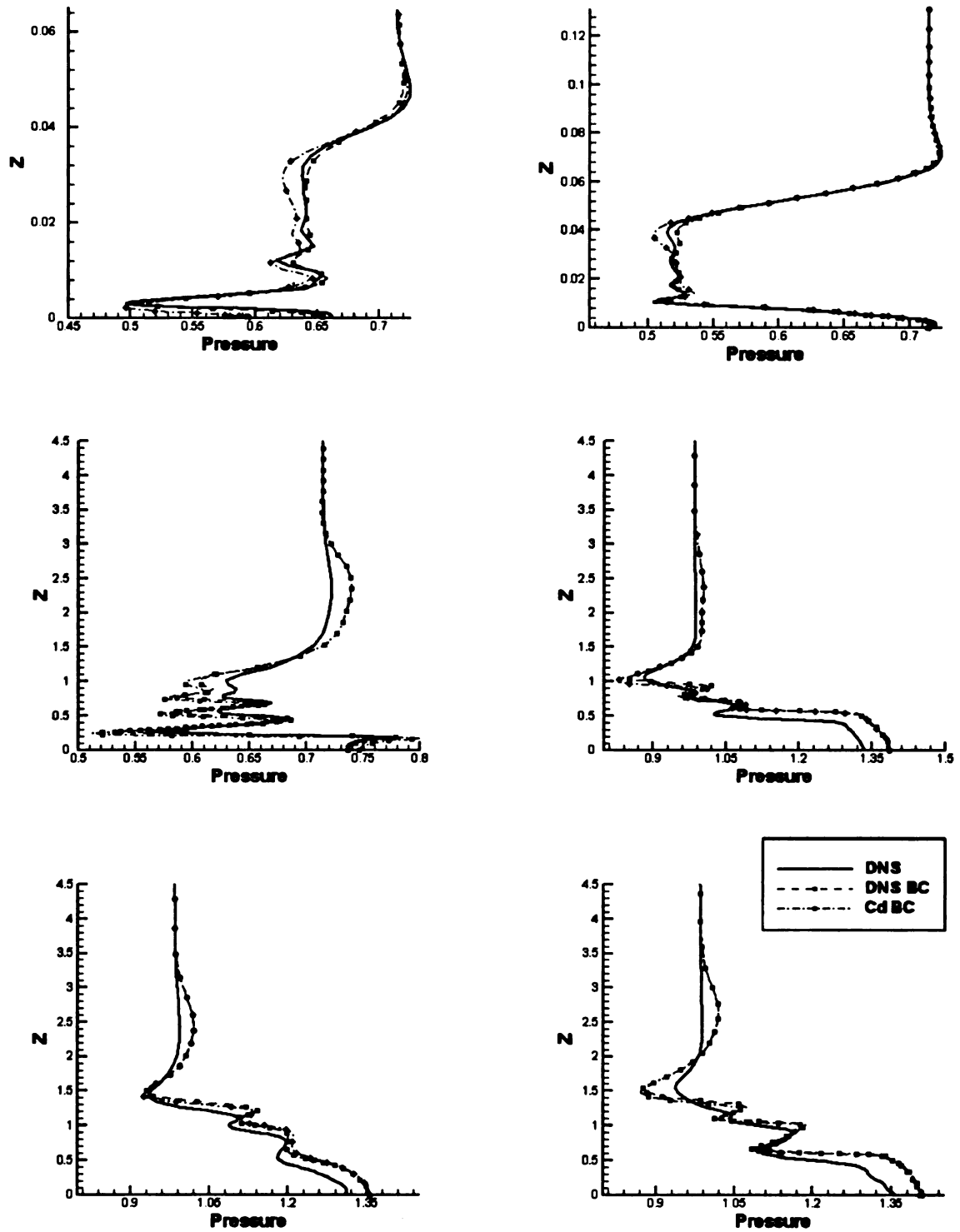


Figure 24: Normalized pressure at 1D downstream of last-row holes for DNS, DNS_BC, and Cd_BC. Same case order as Figure 22.

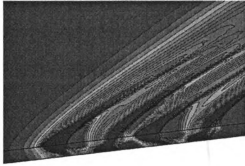
of the DNS results downstream of the last bleed-hole: both boundary conditions perform especially well in the cases without an incident shock (case#1- case#3). The pressure curves for the Cd_BC and DNS_BC boundary conditions also follow the same general pattern as the DNS results downstream of the last hole. For the cases where there was an incident shock, both of the bleed boundary conditions give values for the pressure near the wall that are slightly offset from the DNS results.

With the usefulness of the Cd_BC established, the next objective was to examine the Cd_BC boundary condition on a coarse grid to see if it is able to simulate key effects associated with bleed-hole arrangement and spacing. When testing the Cd_BC on the coarse mesh (one point/cell per normal hole and two points/cells per inclined hole), the value of the discharge coefficient C_D was modified to account for the circular geometry of the bleed hole and the rectangular shape of the cell face. For the coarse mesh, simulations were also performed using the Cd_BC-slot bleed boundary condition: the entire bleed region is treated as a porous wall (i.e., the locations of the bleed holes are not resolved).

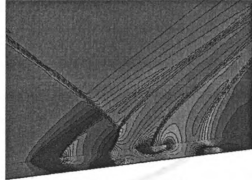
Figures 25 and 26 show the results of the Cd_BC on fine and coarse meshes and the Cd_BC-slot on the coarse mesh for cases 3 and 4. These results are fairly representative of all cases studied involving boundary layers with and without an incident shock. When there is no incident shock, Figure 25 (case 3) shows the Cd_BC on the coarse mesh to still be able to capture some of the effects of the bleed-hole arrangement on the pressure distribution both on and above the surface. The “barrier” shocks, however, are much weaker when compared to the fine mesh case. When there is an incident shock, Figure 25 (case 4) shows that the grid coarsening in the streamwise

direction also coarsened the thickness of the incident shock. Despite this, the coarse mesh was still able to sense some effects of bleed-hole arrangement. Figure 25 clearly shows that with the porous-wall bleed boundary condition, Cd_BC-slot, all of the effects associated with the bleed-hole arrangement are lost.

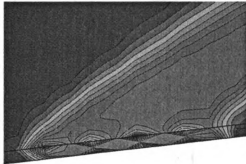
A more quantitative comparison of the Cd_BC on fine and coarse meshes and the Cd_BC-slot on the coarse mesh can be seen in Figure 26. This comparison shows that at 1D downstream of the bleed region, the Cd_BC on the coarse mesh performs well when compared to the results obtained on the fine mesh. The results from the application of the Cd_BC-slot boundary condition are clearly much worse than that from the Cd_BC on the same mesh.



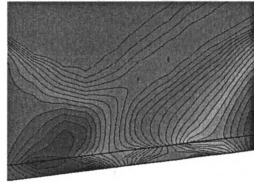
Cd_BC – fine mesh



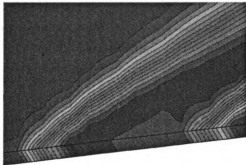
Cd_BC – fine mesh



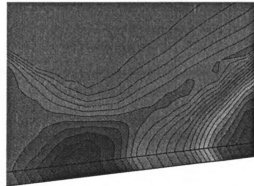
Cd_BC : coarse mesh



Cd_BC : coarse mesh



Cd_BC- slot : coarse mesh



Cd_BC- slot : coarse mesh

Figure 25: Pressure contours in left symmetry plane ($y = L_y$) and on plate surface ($z = 0$) for Cases 3 (left) and 4(right) with Cd_BC on fine and coarse meshes and Cd_BC-slot on coarse mesh.

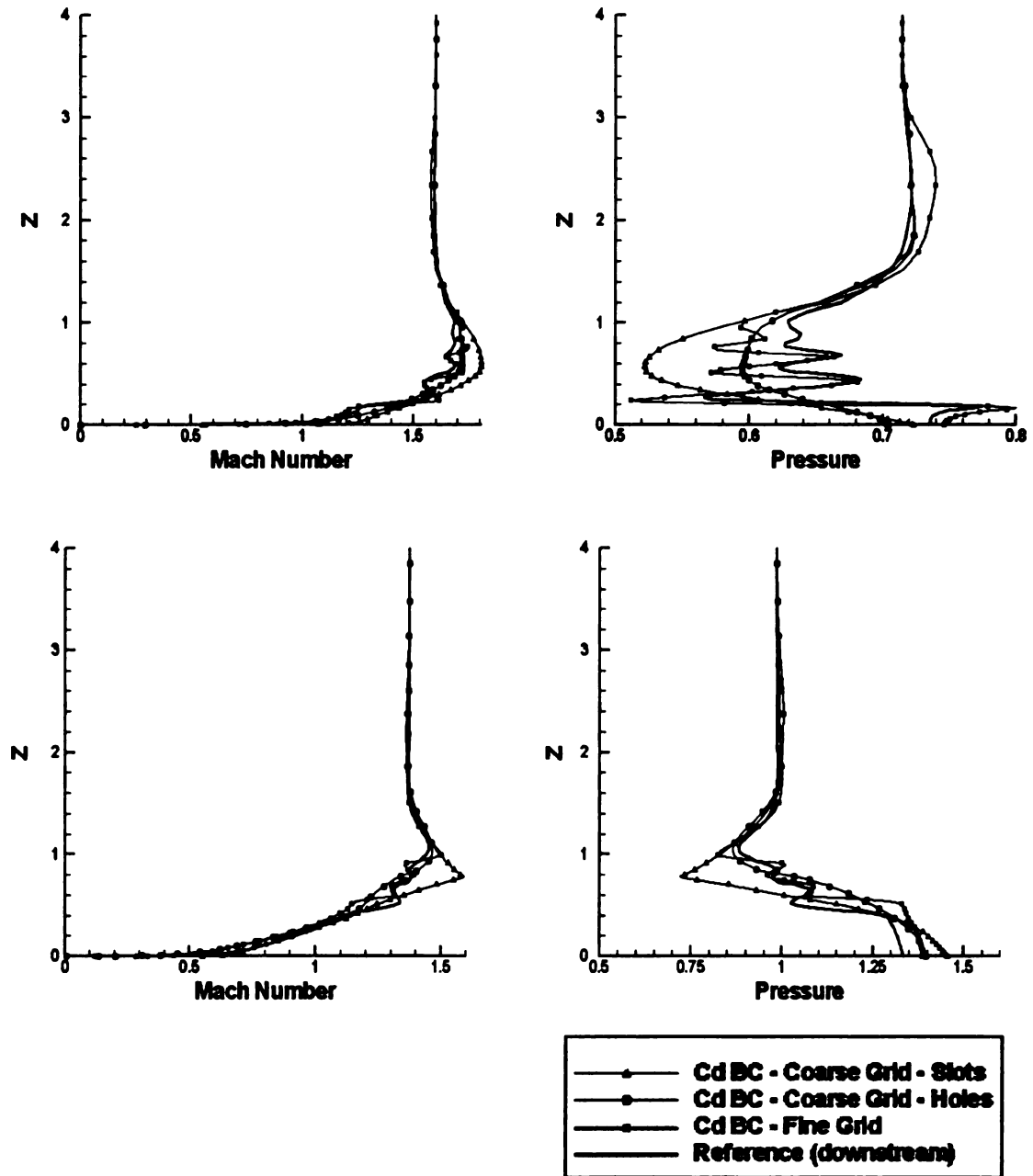


Figure 26: Mach number and pressure profile normal to wall at $y = 0$ and 1D downstream of last row holes for Cases 3 (top) and 4 (bottom) with Cd_BC on fine and coarse meshes and Cd_BC-slot on coarse mesh. 'Reference' refers to DNS results.

Chapter 7

CONCLUSIONS

Four bleed boundary conditions (DNS_BC, W_Avg, Cd_BC, and W_Profile), capable of accounting for the effects of bleed-hole geometry and arrangement, were developed and evaluated in this study. The four boundary conditions were applied to a simulation, where there was supersonic turbulent boundary layer flow over a flat plate and choked bleed through normal bleed holes. The results of these simulations were compared with the results from simulations that resolved the flow through the holes and plenum. Downstream profiles of pressure and Mach number showed little variation among each of the bleed boundary conditions and excellent agreement with the DNS results were obtained. Each of the bleed boundary conditions was also capable of reproducing qualitative features of the bleed process, including the “barrier” shock.

Two of the bleed boundary conditions (DNS_BC and Cd_BC) were then evaluated for six bleed-hole configurations. The results show that the discharge coefficient boundary condition is able to predict accurately both the pressure and Mach number profiles downstream of the bleed region by using only one grid point for a normal bleed hole and two grid points for an inclined bleed hole. The qualitative features of the bleed process including the “barrier” shock can also be discerned. The Cd_BC is shown to be superior to the porous wall bleed boundary condition, Cd_BC-slot, which does not account for the effects of bleed-hole arrangements. The results of this coarse grid study conducted indicate that it is possible to construct a bleed boundary condition by using very few grid points and still be able to capture the key flow physics. The

results also imply that the discharge coefficient is relatively insensitive to the streamwise and spanwise spacing of the holes.

REFERENCES

1. Hahn, T.O., Shih, T.I-P., and Chyu, W.J., "Numerical Study of Shock-Wave/Boundary-Layer Interactions with Bleed," AIAA Journal, Vol. 31, No. 5, 1993, pp. 869-876.
2. Rimlinger, M.J., Shih, T.I-P., and Chyu, W.J., "Three-Dimensional Shock-Wave/Boundary-Layer Interactions with Bleed Through a Circular Hole," AIAA Paper 92-3084, July 1992.
3. Shih, T.I-P., Rimlinger, M.J., and Chyu, W.J., "Three-Dimensional Shock-Wave/Boundary-Layer Interaction with Bleed," AIAA Journal, Vol. 31, No. 10, 1993, pp. 1819-1826.
4. Rimlinger, M.J., Shih, T.I-P., and Chyu, W.J., "Three-Dimensional Shock-Wave/Boundary Layer Interactions with Bleed through Multiple Holes," AIAA Paper 94-0313, Jan. 1994.
5. Chyu, W.J., Rimlinger, M.J., and Shih, T.I-P., "Control of Shock-Wave/Boundary-Layer Interactions by Bleed," AIAA Journal, Vol. 33, No. 7, 1995, pp. 1239-1247.
6. Hamed, A. and Lehnig, T., "Effect of Bleed Configuration on Shock/Boundary Layer Interactions," AIAA Journal of Propulsion and Power, Vol. 11, No. 1, 1995, pp. 42-48.
7. Rimlinger, M.J., Shih, T.I-P., and Chyu, W.J., "Shock-Wave/Boundary-Layer Interactions with Bleed Through Rows of Holes," AIAA Journal of Propulsion and Power, Vol. 12, No. 2, 1996, pp. 217-224.
8. Rimlinger, M.J., Shih, T.I-P., Chyu, W.J., Willis, B.P., and Davis, D.O., "Computations of Shock-Wave/Boundary-Layer Interactions with Bleed," AIAA Paper 96-0432, Jan. 1996.
9. Lin, Y.-L., Stephens, M.A., Shih, T.I-P., and Willis, B.P., "Effects of Plenum Size on Bleeding a Supersonic Boundary Layer," AIAA Paper 97-0609, Jan. 1997.
10. Flores, A.J., Shih, T.I-P., Davis, D.O., and Willis, B.P., "Bleed of Supersonic Boundary-Layer Flow through Rows of Normal and Inclined Holes," AIAA Paper 99-2112, June 1999.
11. Abrahamson, K.W. and Bower, D.L., "An Empirical Boundary Condition for Numerical Simulation of Porous Plate Bleed Flows," AIAA Paper 88-0306, January 1988.
12. Chyu, W.J., Howe, G.W., and Shih, T.I-P., "Bleed Boundary Conditions for Numerically Simulated Mixed-Compression Supersonic Inlet Flows," AIAA Paper

25. Chakravarthy, S.R. and Osher, S., "High Resolution Applications of the Osher Upwind Scheme for the Euler Equations," AIAA Paper 86-1943, 1983.
26. Pulliam, W.R. and Chaussee, D.S., "A Diagonal Form of an Implicit Approximate Factorization Algorithm," Journal of Computational Physics, Vol. 39, 1981, pp. 347-363.
27. Ni, R. H., "A Multiple Grid Scheme for Solving the Euler Equations," AIAA Paper 81-1025, 1981.
28. Anderson, W.K., Thomas, J.L., and Whitfield, D.L., "Multigrid Acceleration of the Flux-Split Euler Equations," AIAA Journal, Vol. 26, No. 6, 1988, pp. 649-654.
29. Benson, D., Shih, T.I-P., Davis, D.O., and Willis, B.P., "Boundary Conditions for CFD Simulations of Supersonic Boundary-Layer Bleed through Discrete Holes," AIAA Paper 2000-0888, Jan. 2000.
30. Benson, D., Shih, T.I-P., Davis, D.O., and Willis, B.P., "Bleed Boundary Conditions for CFD Simulations of Supersonic Flows with Embedded Shocks and Boundary-Layer Bleed," ASME Paper 2001-18116, June 2001.

MICHIGAN STATE LIBRARIES



3 1293 02199 1181